Structural dynamics of the C-terminal X domain of Nipah and Hendra viruses controls the attachment to the C-terminal tail of the nucleocapsid protein

Jean-Marie Bourhis, Filip Yabukarski, Guillaume Communie, Robert Schneider, Valentina Volchkova, Mickaël Frénéat, Francine Gérard, Corinne Ducournau, Caroline Mas, Nicolas Tarbouriech, et al.

Structural dynamics of the C-terminal X domain of Nipah and Hendra viruses controls the attachment to the C-terminal tail of the nucleocapsid protein.

Jean-Marie Bourhis[1#], Filip Yabukarski[1#], Guillaume Communie[1], Robert Schneider[1], Valentina A. Volchkova[3], Mickaël Frénéat[3], Francine Gérard[1], Corinne Ducournau[1], Caroline Mas[2], Nicolas Tarbouriech[1], Malene Ringkjøbing Jensen[1], Viktor E. Volchkov[3], Martin Blackledge[1] and Marc Jamin[1*]

[1]Institut de Biologie Structurale (IBS), Univ. Grenoble Alpes, CEA, CNRS, 71 Avenue des Martyrs, 38000 Grenoble, France.

[2]Integrated Structural Biology Grenoble (ISBG) CNRS, CEA, Univ. Grenoble Alpes, EMBL, 71 avenue des Martyrs, 38000, Grenoble, France.

[3]Molecular basis of viral pathogenicity, Centre International de Recherche en Infectiologie (CIRI), INSERMU1111-CNRS UMR5308, Université Claude Bernard Lyon 1, ENS de Lyon, 69365 Lyon, France.

[#]Co-first authors

Running title: Structure of Nipah virus phosphoprotein X domain

Keywords: Nipah virus, phosphoprotein, Mononegavirales, intrinsically disordered protein, small-angle X-ray scattering, nuclear magnetic resonance, X-ray crystallography

* Corresponding author: Univ. Grenoble Alpes, CEA, CNRS, Institut de Biologie Structurale (IBS), 38000 GRENOBLE.

E-mail : marc.jamin@ibs.fr, Phone: + 33 4 76 20 94 62, Fax : + 33 4 76 20 94 00

ABSTRACT

To understand the dynamic interactions between the phosphoprotein (P) and the nucleoprotein (N) within the transcription/replication complex of the *Paramyxoviridae* and to decipher their roles in regulating viral multiplication, we characterized the structural properties of the C-terminal X domain (P_{XD}) of Nipah (NiV) and Hendra virus (HeV) P protein. In crystals, isolated NiV P_{XD} adopted a two-helix dimeric conformation, which was incompetent for binding its partners, but in complex with the C-terminal intrinsically disordered tail of the N protein (N_{TAIL}), it folded into a canonical 3H bundle conformation. In solution, SEC-MALLS, SAXS and NMR spectroscopy experiments indicated that both NiV and HeV P_{XD} were larger in size than expected for compact proteins of the same molecular mass and were in conformational exchange between a compact three-helix (3H) bundle and partially unfolded conformations, where helix α_3 is detached from the other two. Some measurements also provided strong evidence for dimerization of NiV P_{XD} in solution but not for HeV P_{XD}. Ensemble modeling of experimental SAXS data and statistical-dynamical modeling reconciled all these data, yielding a model where NiV and HeV P_{XD} exchanged between different conformations, and where NiV but not HeV P_{XD} formed dimers. Finally, recombinant NiV comprising a chimeric P carrying HeV P_{XD} was rescued and compared with parental NiV. Experiments carried out *in cellula* demonstrated that the replacement of P_{XD} did not significantly affect the replication dynamics while caused a slight virus attenuation, suggesting a possible role of the dimerization of NiV P_{XD} in viral replication.

Introduction

Nipah virus (NiV) and Hendra virus (HeV) are two emerging zoonotic paramyxoviruses [1,2]. Their natural reservoirs are fruit bats (*Pteropus sp.*) that live in Australia and Southeast Asia [3], but NiV and HeV have the ability to infect numerous other mammals including humans. Although they seem to cause no severe disease in bats, both viruses are highly pathogenic to their new hosts and cause severe encephalitis and/or respiratory illness in humans with lethality ranging from 40 to 90% [4]. There are no vaccines or antiviral therapeutics approved for human use [5] and a risk of person-to-person transmission [6]; they are accordingly classified as Biosafety Level-4 (BSL-4) agents.

NiV and HeV are enveloped viruses with a nonsegmented negative-sense RNA genome. They are classified in the order *Mononegavirales (MNV)*, the family *Paramyxoviridae* and the genus Henipavirus. The genomic RNA and three viral proteins, the nucleoprotein (N), the phosphoprotein (P) and the large RNA-dependent RNA polymerase (L) compose the minimal ribonucleoprotein complex (RNP) that is required for transcription and replication of the viral genome [7,8]. The genomic RNA is packaged into a linear homopolymer of N proteins, forming a long helical nucleocapsid (NC) that serves as template for the L polymerase for both transcription and replication [9,10]. During the infectious cycle, the L polymerase catalyzes RNA polymerization, messenger RNA cap synthesis, cap methylation and polyadenylation [11], while P acts as an essential non-catalytic cofactor of the polymerase [12] and as a chaperone of unassembled N (N^0) [13]. In addition, P also contributes, in synergy with the accessory proteins V, W and C derived from the same P transcription unit, to the strategy of host immune response escape and thus to the pathogenicity of the virus [12,14,15].

Although the sequence of both N and P proteins is poorly conserved between the different genera of *Paramyxoviridae* (10-25% identity for P and 20-40% for N), their overall architecture, the structure of their folded domains and the modalities of their interactions are conserved within the family and the order [16]. The N protein is composed of a core region (N_{CORE}) and of a long C-terminal intrinsically disordered region (N_{TAIL}) (**Figure 1A**) [10,13]. N_{CORE} is mainly composed of two globular domains that are connected by a hinge, creating an RNA binding groove. N_{CORE} also comprises two subdomains, the NT_{ARM} and the $CT_{ARM,}$ that dock to neighboring subunits and stabilize the assembled NC (**Figure 1A**) [10,13]. N_{TAIL} is highly flexible and protrudes from the helical nucleocapsid [17]. The P protein is a modular protein [18] that forms tetramers [12,19]. Each protomer consists of a long N-terminal intrinsically disordered region (P_{NTR}, aa 1–474) and a C-terminal region made of two folded domains, the multimerization domain (P_{MD}, aa 475-580) and the C-terminal X domain, (P_{XD}, aa 655-709), which are connected by a flexible linker ($P_{CT\text{-}LINK}$, aa 581-654) [12] (**Figure 1A**). Owing to the presence of the long disordered regions, NiV P is highly flexible [12].

Throughout the viral replication cycle different interactions occur between paramyxovirus P and N proteins involving different regions of both proteins. Two main interactions have been described for a long time, but the recent discoveries of several additional weak binding interactions revealed a more complex and dynamical network of contacts between both

proteins (green arrows in **Figure 1A**): (i) *Binding interaction 1 (BI_1 in Figure 1A)*: P_{NTR} contains a N^0 chaperone module (P_{CM} - aa 1–35) at its N-terminal end that binds the C-terminal domain of N_{CORE} in the unassembled RNA-free N^0. This chaperone module is a molecular recognition element or MoRE (*i.e.* an intrinsically disordered region that adopts a stable fold upon binding to its partner [20]) that is globally disordered with fluctuating α-helical elements in isolated P [12], but that adopts a stable conformation when it binds to its N^0 partner [13]. (ii) *Binding interaction 2 (BI_2 in Figure 1A)*: The C-terminal folded X domain (P_{XD} - aa 655-709) binds to a conserved MoRE in N_{TAIL}, thus mediating the attachment of P to N, in particular to the nucleocapsid [21–23], but also potentially to N^0. This interaction was shown to be dispensable for the functioning *per se* of the polymerase with some truncated forms of both N and P proteins [24], but it appeared essential for controlling the replication process [25] and for the formation of membrane-less organelles in host cells, [26,27]. (iii) *Additional* w*eak binding interactions*: A weak binding region for N^0 (wBI_1) was recently identified in measles virus P_{NTR} (HELL box), which is conserved in NiV and likely plays a role in the chaperone function of P [28]. Another weak interaction was found between the P_{XD} bound to N_{TAIL} and N_{CORE} (wBI_2), which controls the replication dynamics [29], and another one between the $P_{CT\text{-}LINK}$ and an unidentified region of N (wBI3), which controls the dynamics of the formation of liquid compartments [26]. The N and P proteins and their interactions are potential targets for new therapeutic approaches [30].

The dynamics of the interplay between P_{XD} and N_{TAIL} is thought to play a key role in the mechanisms of transcription, replication and encapsidation by connecting P and L to the nucleocapsid [31–33]. Thus, it allows the polymerase (i) to load at the 3' end of the template nucleocapsid, (ii) to remain attached to the template nucleocapsid while it progresses along genomic RNA [32] and (iii) in particular when it scans intergenic regions thereby regulating the transcription gradient [24,25,34]. It also allows to deliver unassembled nucleoprotein (N^0) to the site of viral RNA synthesis [13]. However, recent experiments with different paramyxoviruses have led to a modification of this scenario involving additional roles for the interaction between N_{TAIL} and P_{XD} [25,34,35]. Firstly, the flexible N_{TAIL} regions are localized on the outer side of the helical nucleocapsid [36,37] and they collectively act like a molecular brush that repels any incoming molecules including the polymerase complex and thus prevents the interaction between L and its template. An ingenious mutational study suggested that the binding of P_{XD} to the central MoRE of N_{TAIL} displaces the N_{TAIL} chains from the nucleocapsid core, allowing L to access the 3' end of the genome and to move along the template [24,25,38]. Secondly, the interaction between N_{TAIL} and P_{XD} has been shown to be essential for keeping the polymerase complex attached to the template as it scans the intergenic regions, promoting the re-initiation at the next gene-start signal and thus controlling the transcription gradient [25,34]. Thirdly, mutational experiments has revealed that the strength of the interaction between N_{TAIL} and P_{XD} controls the rate of RNA synthesis by regulating the speed of the polymerase motion along the template [35]. Even if the strength of the interaction is not proportional to the rate of RNA synthesis, stronger binding reduces polymerase activity, suggesting that the interaction between N_{TAIL} and P_{XD} acts as a brake on RNA polymerization [35,39,40]. Fourthly, a transient interaction between the N_{TAIL}-P_{XD}

complex and N_{CORE} has been proposed to stimulate the dissociation step and thus the progress of P along the nucleocapsid template [41]. Finally, the interactions between N_{TAIL} and P_{XD} and between $P_{CT\text{-}LINK}$ and N_{CORE} are indispensable for forming viral factories by inducing liquid-liquid phase separation [42]. Additionally, a complex dynamical network of interactions also controls the binding of paramyxovirus P to the L polymerase. A binding site was initially localized in the C-terminal part of P_{MD} and a short segment of $P_{CT\text{-}LINK}$ [43], but recent studies showed that P_{XD} also directly binds to the polymerase [44,45], possibly influencing the interactions with N (orange arrows in **Figure 1A**).

To understand the dynamical interplay between P and N within the *Mononegavirales* transcription/replication complex and to decipher its role in regulating viral multiplication, we set out to characterize the structure of NiV P_{XD} alone and in complex with a peptide encompassing the central MoRE of N_{TAIL}. Surprisingly, the isolated NiV P_{XD} crystallized in a non-canonical fold, which is incompetent for binding N_{TAIL} or the L polymerase, whereas the domain adopts a canonical three-helix bundle (3H) fold in the complex with N_{TAIL}. To further investigate this conformational change, we used size-exclusion chromatography coupled to multi-angle laser light scattering (SEC-MALLS) and small-angle X-ray scattering (SAXS) to compare the oligomerization state and average size of NiV and HeV P_{XD} in solution and found that both domains undergo conformational exchange and that NiV P_{XD} displays propensity to dimerize but not HeV P_{XD}. By NMR exchange experiments on NiV P_{XD}, we confirmed the existence of a canonical three-helix (3H) bundle in conformational equilibrium with a less populated elongated two-helix (2H) hairpin, and by ensemble modeling of experimental SAXS data we generate models where both NiV and HeV P_{XD} exchange between the 3H and 2H conformations, and that the NiV but not HeV P_{XD} equilibrium is concentration dependent. We devised a statistical thermodynamic model of the interaction between polymeric P and N to study the effect of the tetramerization of P on the enhancement of the binding to the polymeric N-RNA complex by an avidity effect, and to evaluate the impact of both P_{XD} conformational change and dimerization on the binding to N_{TAIL}. Finally, to further investigate the role of the propensity of NiV P_{XD} to dimerize, we rescued a recombinant NiV comprising a chimeric P protein, where we replaced NiV P_{XD} by HeV P_{XD} (equivalent to 12 point mutations). Our experiments *in cellula*, showed that chimeric recombinant NiV replicated comparably well in susceptible cell lines while revealing slight attenuation in comparison with the parental NiV, supporting a role of the dimerization of NiV P_{XD} in viral replication.

Results

Crystal structure of isolated NiV P_{XD} reveals a noncanonical fold

The C-terminal X domain of NiV P (P_{XD}: aa 655-709) fused to a C-terminal His6 tag was expressed in *E. coli* and purified by affinity and size exclusion chromatography. The protein crystallized with one molecule in the asymmetric unit, and crystals diffracted up to 2.1 Å resolution. Despite a high level of sequence identity with HeV P_{XD} (78 % identity) (**Figure 1B and Supplemental Figure 1A**), the structure could not be solved by molecular

replacement using either the known HeV P_{XD} crystal structure [23] or any other known paramyxovirus P_{XD} structure as search model [21,46–48]. However, we were able to solve NiV P_{XD} structure by the SIRAS method [49] (**Table 1**) (PDB code:7PON) (**Figure 1C**).

Unexpectedly, the crystal structure of NiV P_{XD} is different from the canonical compact three-helix (3H) bundle structure found for other known *Paramyxoviridae* P_{XD} [23,47,50]. NiV P_{XD} forms a two-helix (2H) hairpin with one short helix α_1 and one long helix $\alpha_{□-3}$, both clearly visible in the experimental electron density map (**Figure 1C**). Sequence-based superposition of NiV P_{XD} structure to the previously determined HeV P_{XD} 3H bundle [23] shows that the NiV helix α_1 and the N-terminal part of helix α_{2-3} aligned to HeV helices α_1 and α_2 (**Figures 1B and 1D**). The linker that connects α_2 and α_3 in HeV P_{XD} (shown in blue in **Figure 1D**) forms an additional α-helical turn in NiV P_{XD} (shown in gray in **Figure 1D**), leading to the long C-terminal α_{2-3}. The interface between α_1 and $\alpha_{□-3}$ is hydrophobic and consists of two layers of side-chains. One layer composed of Arg661, Ile664, Ile668, Ile672, Leu677, Leu681, Ile682, Y684 and Leu685 forms a flat, solvent-exposed, hydrophobic surface (Face A in **Supplemental Figure 2A)**. The other layer composed of Lys665, Arg669, Arg675 and Arg678 forms an irregular positively charged surface (Face B in **Supplemental Figure 2A**). A network of salt bridges and H-bonds connects Arg661 and Lys665 side-chains at the N-terminus of α_1 with Gln685, Glu689 and Glu692 side chains located in the middle of α_{2-3}, likely stabilizing the additional helical turn that allowed the extension of α_{2-3} to the C-terminal extremity of the protein (**Figure 1E**). The C-terminal part of α_{2-3}, which makes no tertiary contacts, is amphipathic with eight residues (Ile694, Ile697, Ala698, Val701, Ile704, Ile705, Ile709) forming a hydrophobic side of the helix, and ten polar residues (Glu692, Gln694, Glu695, Asn699, Thr700, Gln702, Asp703, Asp706, and Asn708) forming a hydrophilic, negatively charged side (**Supplemental Figure 2A**). No clear electron density was seen for the His6 tag.

Inspection of the crystal packing revealed that two NiV P_{XD} molecules, related by a crystallographic symmetry axis, formed a dimer stabilized by extensive contacts (**Figure 1F**). The dimerization interface consisted of the flat hydrophobic surface formed by helix α_1 and the N-terminal half of helix α_{2-3} of each molecule. Analysis of this interface with PISA [51] and Eppic [52] revealed a buried surface area of ~600 Å² in line with a natural protein-protein interaction rather than with a state created by crystal packing constraints. In addition, one specific polar contact was formed between the side chain hydroxyl group of Ser660 of each monomer and the backbone carbonyl of His671 of the facing symmetry mate (**Figure 1F**). The distance of 3.5 Å between these groups was compatible with the formation of H-bonds, which might provide additional stabilization to the dimer. The formation of the dimer prevented the docking of helix α_3 onto the hairpin formed by helices α_1 and α_2, and thus prevented the formation of the canonical 3H bundle structure. In consequence, the absence of the surface formed by helices α_2 and α_3 prevented the interaction with N_{TAIL}, and thus dimerization interfered with the attachment of P onto the NC. It is also noteworthy that the C-terminal part of helix α_{2-3} interacts with three other protomers related by crystal symmetry,

likely explaining the presence of this long helix in the crystal, but all these interfaces are classified as crystallographic contacts by PISA [51] and Eppic [52] (Supplementary figures 2B-C).

NiV P_{XD} adopts a compact three-helix bundle upon interacting with its physiological partner N_{TAIL}

One role of P_{XD} in the *Paramyxoviridae* replication machine is to connect P to N through direct interaction with a MoRE located in N_{TAIL} [21,23,53,54]. Multiple sequence alignments showed that N_{TAIL} is less conserved than N_{CORE} (**Supplemental Figure 1A**), but revealed the presence of three conserved regions in Henipavirus N_{TAIL} (**Figure 2A**), named boxes 1 to 3, as described for the closely related genus Morbillivirus [55]. The three conserved boxes were predicted to be MoREs [56], and the interaction of Box 2 with P_{XD} was documented in several studies [23,37,57–59].

To solve the crystal structure of the complex, we followed a strategy similar to that used by Matthews and coworkers for solving the structure of the corresponding complex of MeV [21], and constructed a chimeric protein in which residues 473 to 495 of N ($N_{473-495}$) were fused to P_{XD} ($P_{655-709}$) through a flexible [$(GS)_4G$] linker (**Figure 2B**). We expressed the chimeric protein including a C-terminal His6 tag in *E. coli* and purified it by affinity chromatography and size exclusion chromatography. The protein crystallized with seven molecules in the asymmetric unit, and crystals diffracted up to 2.7 Å resolution (**Table 1**). As for isolated NiV P_{XD}, we could not solved the structure by molecular replacement with any known P_{XD} structure as search model, but we obtained initial crystallographic phases through a combinatorial approach in which we generated 10,000 *ab initio* models of NiV P_{XD} with Rosetta [60] and performed automated molecular replacement with the Ample procedure implemented in CCP4 [61]. In this process, we excluded N_{TAIL} from the search model such that the presence of a well-defined electron density corresponding to residues 473 to 486 of N (473-TNSLLNLRSRLAAK-486) in all seven molecules of the asymmetric unit validated the structure and allowed us to orient unambiguously the N_{TAIL} fragment (**Figure 2C**). In five molecules present in the asymmetric unit, a clear electron density was visible for the backbone of a few additional residues at the C-terminal end of the α-MoRE, and we were able to build a model up to residue 492, although the electron density for the corresponding side chains was poorly defined (**Table 1**) (PDB code: 7PNO). The first Gly residue of the linker was visible at the C-terminal end of helix α_3, whereas the last four residues of the linker (SGSG) were visible at the N-terminal extremity of the N_{TAIL} helix.

In association with N_{TAIL}, NiV P_{XD} adopted the typical antiparallel 3H bundle fold with an up-down-up topology (**Figure 2D**). The long helix α_{2-3} found in the crystal structure of isolated P_{XD} was interrupted at residue Lys687, residues 688-690 formed a loop (shown in gray in **Figure 2D**) and residues 691-705 formed the third helix α_3. The latter packed on the flat hydrophobic surface created by helices α_1 and α_2. Residues 473-490 of N_{TAIL} formed a fourth

helix, α_N, which packed on the surface created by helices α_2 and α_3 of P_{XD}, forming a four-helix bundle with an up-down-up-down topology (**Figure 2D**). Given that only 4 residues of the linker connecting N_{TAIL} to P_{XD} (9 residues) were missing in the electron density map and the distance of 0.9 nm (ranging from 0.85 to 0.93 in the 7 molecules of the asymmetric unit) separating the C-terminal extremity of P_{XD} from the N-terminal extremity of N_{TAIL}, we could definitely rule out swapping of N_{TAIL} between adjacent molecules in the crystal packing.

Structural alignments of NiV P_{XD} 3H form with the P_{XD} from other paramyxoviruses revealed a very similar fold with root-mean-square deviations (r.m.s.d.) of the Cα atomic coordinates of 0.68 Å for HeV P_{XD}, 1.27 Å for MeV P_{XD} and 1.42 Å for SeV P_{XD}. However, the position of N_{TAIL} relative to P_{XD} was different from that found in the corresponding MeV N_{TAIL}-P_{XD} complex [21] (**Figure 2E**). In the NiV structure, the helix α_N was parallel to helix α_2 and antiparallel to helices α_1 and α_3, thus adopting an opposite orientation than helix α_N in the MeV structure [21]. We could clearly identify several residues in the electron density map and thus unambiguously established the orientation of the peptide chain (**Supplemental Figure 2D**). In addition, although the packing angles between helix α_N and helix α_2 (-150°) or helix α_3 (+10°) were similar to those found in the MeV complex, the tilt angle formed by helix α_N axis with respect to the plane defined by helices α_2 and α_3 was larger than that found in the MeV complex [21].

The analysis of the binding interfaces with PISA [51] revealed a buried surface area of 960 Å² between N_{TAIL} and P_{XD}, smaller than that of 1270 Å² accompanying the formation of the MeV complex [21]. The binding interface of NiV P_{XD} consisted of a central hydrophobic groove (Leu677, Leu681, Tyr684, Ile697, Ile704) flanked by negatively charged ridges (Glu680, Glu689, Glu693, Glu696, Asp703, Asp706), creating areas of negatively charged surface (**Supplemental Figure 3**). The facing interface on N_{TAIL} contained a central ridge made of three hydrophobic residues (Leu476, Leu479, Leu483) that inserted into the hydrophobic groove of P_{XD}. Three charged residues (Arg480, Arg482 and Lys 486) on the sides created positive surface areas, which interacted with the negative surface areas of P_{XD}. The contacts between P_{XD} and N_{TAIL} involved residues composing the conserved Box 2 within the genus Henipavirus (**Figure 2A**). In addition, Glu680 in P_{XD} formed salt bridges with Arg480 in N_{TAIL} (**Figure 2F**), whereas Asp703 in P_{XD} formed H-bonds with Ser475 in N_{TAIL} (**Figure 2G**), respectively, specifically locking the two proteins in register. Depending on the protomer in the asymmetric unit, Lys486 in N_{TAIL} forms a salt bridge with either Glu693 or Glu696 (not shown). Also, the δ1 methyl group of Leu483 in N_{TAIL} was positioned in front of Tyr684 aromatic ring suggesting a methyl-π interaction [62] (**Figure 2F**). All hydrophobic and polar residues involved in both interfaces were strictly conserved in HeV, with the exception of residue 697, which was an isoleucine in NiV and a valine in HeV, explaining the cross reactivity observed between NiV and HeV [59]. A comparison of N_{TAIL}-bound NiV P_{XD} with free HeV P_{XD} revealed a different orientation of Tyr684, whereas a comparison with P_{XD} from other viruses revealed specific patterns of contacts most likely preventing cross reactivity (**Supplemental Figure 3**)

NiV and HeV P_{XD} partially unfold in solution

The comparison of the free and N_{TAIL}-bound NiV P_{XD} structures raised questions about the conformation adopted by this domain in solution. Three different structures of NiV P_{XD} could be considered from our new crystal structures – a monomeric 2H form (2H), a dimeric 2H form ($2H_{Dim}$) and a monomeric 3H form (3H) – which made different predictions with respect to their molecular dimensions and molecular mass in solution. We thus performed SEC-MALLS experiments, which provide independent measurements of the hydrodynamic radius (R_h) from the elution volume and of weight average molecular mass (M_w) from the light scattering intensity. The M_w of 6.5 ± 0.1 kDa and 6.6 ± 0.3 kDa determined for NiV and HeV P_{XD} from experiments performed at a typical protein concentration of 5 $mg.mL^{-1}$ were in agreement with the calculated values for the monomers (6,299 Da and 6,332 Da), respectively (**Figure 3A**). However, NiV and HeV P_{XD} eluted before RNAse A (R_h = 1.95 ± 0.02 nm; mass = 13.7 kDa) and their R_h values of 2.02 ± 0.02 nm and 1.97 ± 0.02 nm determined by calibrating the column with standard globular proteins suggested that, in solution, both domains were not globular or oligomeric (**Figure 3A**). Moreover, the R_h values of NiV and HeV P_{XD} were comparable indicating a similar hydrodynamic behavior for both domains in solution.

The far-UV circular dichroism (CD) spectrum of both NiV and HeV P_{XD} exhibited minima at 208 and 222 nm typical of the presence of α-helices. The average helical content of ~66% estimated from the CD value at 222 nm was in good agreement with the fraction of helical residues found in the crystal structures of NiV (~70 %) and HeV (~63%) P_{XD} (**Figure 3B**).

To further characterize the structure of NiV P_{XD} in solution, we carried out the backbone spectral assignment of the protein and calculated its secondary structure propensities (SSP) [63]. The chemical shift assignments clearly showed that the 3H bundle structure was predominant in solution (**Figure 3C**), although the NMR spectra also showed signs of a minor form. This was most apparent for the C-terminal resonance I709, which showed two separate resonances corresponding to the major 3H bundle structure and a minor conformation (**Figure 3D**). Slow conformational exchange was observed between the two states as evidenced by exchange cross peaks in the ^{1}H-^{15}N HSQC spectrum (**Figure 3D**). To explore the nature of the minor conformation in more detail, we carried out ^{15}N chemical exchange saturation transfer (CEST) experiments [64]. Most of the residues located in helix α_1 and the N-terminal part of helix α_2 did not show conformational exchange or displayed a very small chemical shift difference between the minor and the major state. Residues located in helix α_3 and in the C-terminal part of helix α_2 (residues 684 to 709) showed moderate or large chemical shift changes between the minor and major state (**Figure 3E**). We fitted the CEST data for these residues simultaneously according to a two-site exchange model (**Figure 3F**) providing a population of the minor state of p_{minor} = 9.9 ± 0.2% and an exchange rate of k_{EX} = 169 ± 5 s^{-1}. Note that although appearing with large errors in the optimized parameters, the difference in transverse relaxation rate, ΔR_2, between the major and the minor states was negative for most

residues within helix α_3 suggesting an increased level of dynamics in the minor state for these residues. To investigate whether the minor conformation corresponded to an unfolding of helix α_3, we compared the differences in chemical shifts between the major and the minor states to the difference between the experimental ^{15}N shifts of the major state and those of tabulated ^{15}N random coil shifts [65]. Excellent correlation was observed between the shifts (**Figure 3E**) with the only outliers corresponding to residues in the C-terminal end of helix α_2. These results demonstrated that the minor state transition observed by NMR corresponded to unfolding of helix α_3 and that the residues in the C-terminal part of helix α_2 experienced chemical exchange due to this unfolding, but that helix α_2 remained intact. In conclusion, NiV P_{XD} undergoes slow exchange between the 3H bundle structure (~90 % population) and a 2H hairpin structure where helix α_3 is unfolded (~10 % population).

Thermal unfolding experiments monitored by far-UV CD at 222 nm corroborated the marginal stability of both NiV and HeV P_{XD} domains and the partial unfolding of a fraction of the molecules at room temperature (**Figure 3G**). The thermal unfolding up to 90 °C was fully reversible for both protein domains. The sigmoidal shape of the curves indicated a cooperative behavior typical of a small protein with a hydrophobic core. HeV P_{XD} was more stable than NiV P_{XD}, with T_m values of 53.5 ± 0.2 °C (ΔH^0_{unf} = 35.0 ± 0.7 kcal.mol^{-1}) and 42.5 ± 0.3 °C (ΔH^0_{unf} = 25.3 ± 0.4 kcal.mol^{-1}), respectively. Clearly, at 20°C, NiV P_{XD} was at the beginning of its unfolding transition, whereas HeV P_{XD} was still in the pre-transition region (dotted line in **Figure 3G**).

NiV P_{XD} exists in a monomer-dimer equilibrium in solution

To test the possible oligomerization of NiV and HeV P_{XD}, we performed SEC-MALLS experiments at varying protein concentrations. For NiV P_{XD}, but not for HeV P_{XD}, we clearly observed concentration-dependent increases of R_h and M_w values (**Figures 4A and 4B**). The elution volume of NiV P_{XD} varied from 12.5 mL for an injected concentration of 0.04 mg.mL^{-1} to 11.9 mL for a concentration of 48 mg.mL^{-1} (**Figure 4A**) corresponding to an increase of the R_h value from 2.0 ± 0.05 nm to 2.2 ± 0.05 nm (**Supplemental Figure 4A**). The signal-to-noise ratio of scattered light allowed precise Mw determination only for samples at initial concentrations equal or higher than 5 mg.mL^{-1}, for which M_w increased from 6.3 ± 0.4 kDa (5 mg.mL^{-1}) to 7.6 ± 0.3 kDa (48 mg.mL^{-1}) (**Supplemental Figure 4A**). In addition, at high P_{XD} concentration, the shape of the elution peak was clearly asymmetric revealing rapid and reversible equilibrium between several species (**Figure 4A**). For HeV, the elution volume of 12.6 mL (R_h = 2.0 ± 0.05 nm) and the calculated Mw of 6.6 ± 0.4 kDa showed no significant variations within the tested range of injected concentrations (5 to 33 mg.mL^{-1}) (**Figure 4B**), although it is possible that the dilution of the protein solution upon separation by SEC masked a reversible oligomerization at high HeV P_{XD} concentrations.

To further characterize the oligomerization process of NiV P_{XD} and investigate a possible oligomerization of HeV P_{XD} at high concentration, we recorded SAXS data for scattering

vectors (Q) ranging from 0.05 to 3.0 nm^{-1} at concentrations ranging from 2.5 to 20.0 $mg.mL^{-1}$ for NiV P_{XD} and from 2.0 to 18.0 $mg.mL^{-1}$ for HeV P_{XD}. The normalized scattering profiles at low and high concentrations of NiV P_{XD} were different (**Figure 4C**). The slope and intercept of the normalized Guinier plots drawn for Q values in the range of $Q.R_g < 1.3$ changed with protein concentration (**Figure 4D**). The R_g value increased from 1.47 ± 0.05 nm (2.0 $mg.mL^{-1}$) to 1.80 ± 0.04 nm (20.0 $mg.mL^{-1}$) (**Figure 4G**), while the molecular mass calculated from the scattered intensity at zero angle (I_0/C) increased from 7.4 ± 0.4 kDa (2.0 $mg.mL^{-1}$) to 11.6 ± 0.03 kDa (20.0 $mg.mL^{-1}$) (**Figure 4H**). We fitted the dependency of I_0/C on protein concentration according to monomer-dimer equilibrium and K_d value of 2.8 ± 0.4 $mg.mL^{-1}$ μM (~ 440 μM) assuming a molecular mass at infinite dilution equal to that of the monomer (**Figure 4H**).

By contrast, the normalized scattering profiles at low and high concentrations of HeV P_{XD} were almost superimposable (**Figure 4E**). The normalized Guinier plots drawn for Q values in the range of $Q.R_g < 1.3$ were similar (**Figure 4F**), while the R_g and molecular mass values displayed only minor changes with protein concentration (**Figures 4G and 4H**), confirming the absence of (or a weak) dimerization in this extended concentration range. At infinite dilution, the molecular mass of 6.5 ± 0.5 kDa derived from the normalized scattering intensity at zero angle (I_0/C) (**Figure 4H**) was close to the theoretical MM value of 6.332 kDa, while the R_g value of 1.38 ± 0.03 nm (**Figure 4G**) was larger than that of 1.15 nm calculated for the crystal HeV 3H bundle conformation [23]. We fitted the dependency of I_0/C on protein concentration according to monomer-dimer equilibrium and obtained a K_d value larger than 190 ± 20 $mg.mL^{-1}$ (~ 30 mM) (**Figure 4H**). At low protein concentration, both NiV and HeV P_{XD} were mainly in their monomeric form, but their scattering profiles were slightly different (**Figure 4I**), and both NiV and HeV domains were larger in size than expected for a globular 3H fold in accordance with the partial unfolding of helix α3 unveiled by NMR spectroscopy (see above).

Finally, evidence for a monomer-dimer equilibrium of NiV P_{XD} was also obtained in a SEC-SAXS experiment (**Figure 4J**). The SAXS profile recorded at the center of the elution peak (frame 181) was significantly different from the profiles recorded ahead (frame 167) or behind the elution maximum (frame 208) (**Figures 4K and L**), while the radius of gyration calculated at low Q values by using the Guinier approximation varied across the elution peak, reaching a maximum at the center of the eluting peak (**Figure 4J**). These results suggested that the dimer was partially dissociated at low concentration (in the front and rear parts of the elution peak) and that the kinetics of the monomer-dimer exchange were fast in comparison to the minute timescale of the chromatographic separation.

In conclusion, our results showed that both NiV and HeV P_{XD} undergo conformational exchange and form heterogeneous ensembles of conformers in which a fraction of the molecules are partially unfolded, and that NiV P_{XD} differs from HeV P_{XD} in its capacity to form dimer in a concentration-dependent equilibrium.

Conformational ensembles modeling of NiV and HeV P_{XD}

In Figures 5A to 5C, we compared the experimental scattering profile of NiV P_{XD} at a concentration of 8.0 $mg.mL^{-1}$ with the theoretical profiles calculated with CRYSOL for the different crystal forms available. In this approach, we simply scaled the curves to compare their shape without accounting for possible differences in molecular masses. The overall shape of the experimental curve was different from the theoretical curves calculated for the monomeric 3H bundle form extracted from the crystal structure of the chimeric P_{XD}-N_{TAIL} (**Figure 5A**), for the monomeric 2H form (**Figure 5B**) and for the dimeric $2H_{Dim}$ form extracted from the crystal structure of isolated P_{XD} (**Figure 5C**). Similarly, in **Figure 5D**, we compared the experimental scattering profile of HeV P_{XD} at a concentration of 9.0 $mg.mL^{-1}$ with the calculated profiles for the 3H fold extracted from the crystal structure [23] and with a 2H form of NiV P_{XD}. The comparisons at other protein concentrations are shown in **Supplemental figures 4B**. These results confirmed our hypothesis of the coexistence of multiple conformers in solution.

To obtain a comprehensive view of the conformational heterogeneity in solution, we turned to ensemble modeling, applying the Ensemble Optimization Method (EOM) to our SAXS data [66–68]. This approach consists in generating a large initial pool of physically accessible independent conformers of the molecule with the software RANCH, which creates random conformations of the alpha-carbon trace based upon the sequence, and in selecting sub-ensembles of conformers that collectively reproduce the experimental SAXS curve with the software GAJOE [66]. We generated an initial ensemble of 70,000 P_{XD} conformers by assembling seven sub-ensembles of 10,000 conformers (**Figure 5E**): (i) A sub-ensemble of monomeric 3H bundle models (Pool 1) based on the crystal structure of NiV chimeric P_{XD}-N_{TAIL} structure, in which only the N- and C-termini segments were allowed to adopt different conformations. (ii) Three sub-ensembles of flexible monomeric 2H hairpin models based on the crystal structure of NiV P_{XD}, in which the C-terminal part of the long helix $\alpha_{2\text{-}3}$, the loop connecting α_1 to $\alpha_{2\text{-}3}$ and the N- and C-termini segments were allowed to adopt different conformations. The C-terminal part of the long helix $\alpha_{2\text{-}3}$ was either maintained in its helical conformation and position relative to the N-terminal part (Pool 2), or maintained in its helical conformation but allowed to move relative to the N-terminal part (Pool 3) or allowed to adopt random conformations (Pool 4). (iii) A sub-ensemble of dimeric models based on the crystal structure of isolated NiV P_{XD}, in which only the N- and C-termini segments were allowed to adopt different conformations (Pool 5). (iv) Two sub-ensembles of flexible dimeric models based on the crystal structure of isolated NiV P_{XD}, in which the C-terminal part of the long helix $\alpha_{2\text{-}3}$, the loop connecting $\alpha 1$ to $\alpha_{2\text{-}3}$ and the N- and C-termini segments were allowed to adopt different conformations. The C-terminal part of the long helix $\alpha_{2\text{-}3}$ was either maintained in its helical conformation (Pool 6) or allowed to adopt random conformations (Pool 7). For the sake of simplicity, we report the results of our analysis by clustering the selected decoys into three sets: monomeric 3H bundle (Set 1 = Pool 1), monomeric 2H conformers (Set 2 = Pools 2 to 4) and dimeric $2H_{DIM}$ conformers (Set 3 = Pools 5 to 7).

We fitted the SAXS curves obtained for HeV P_{XD} at 2.5 mg.mL^{-1} and for NiV P_{XD} at four different protein concentrations (2.5, 5.0, 8.0 and 20.0 mg.mL^{-1}) with this method (**Figures 5F-J**). For HeV P_{XD}, only monomeric conformers were selected supporting a model where the compact 3H (55 %) form was in equilibrium with the partially unfolded 2H forms (45 %) (**Figures 5E and 5F**). For NiV P_{XD}, mixtures of monomeric and dimeric forms were selected. According to our other results, the equilibrium for NiV P_{XD} was dependent on protein concentration. At 2.5 mg.mL^{-1}, the monomeric states accounted for 80% with a large fraction of monomeric compact 3H bundle conformers (72 %) and only 8% of the more extended 2H conformers (**Figures 5E and 5G**). Increasing NiV P_{XD} concentration resulted in a shift of equilibrium such that, at 5, 8 and 20 mg.mL^{-1}, the fraction of selected dimeric models increased to 40 %, 44 % and 80 %, respectively (**Figures 5E and 5G-J**). Multiple rounds of selections yielded similar results as attested by the size of the error bars shown in **Figure 5E**. At a protein concentration of 8 mg.mL^{-1}, the 7% population of monomeric 2H conformers in the EOM selection were in agreement with the 10% determined from the NMR CEST data (**Figure 3F**). Note that the CEST experiments are sensitive to slow conformational exchange processes (milliseconds) and that the formation of P_{XD} dimers must occur on a time scale, which is too fast to be detected by CEST.

The interaction of NiV P_{XD} with N_{TAIL} prevents dimerization

To investigate the role of N_{TAIL} in controlling the dimerization of P_{XD}, we carried out SEC-MALLS and SEC-SAXS experiments with the NiV N_{TAIL}-P_{XD} fusion protein (**Figures 6AB**). No concentration dependence was observed by SEC-MALLS, and the experimental M_w of 11.0 ± 1 kDa calculated from the experimental data was in agreement with the theoretical molecular mass of the monomer (10.2 kDa) (**Figure 6A**). The protein eluted from the SEC column before NiV P_{XD} and RNAse A, suggesting the presence of flexible regions (**Figure 6A**).

In the SEC-SAXS experiment, the protein eluted as a single peak **(Figure 6B)**. In contrast to the results obtained with P_{XD} alone (**Figure 4J**), the R_g value determined by using the Guinier approximation at low Q values was constant throughout the elution peak **(Figure 6B)**. This confirmed the absence of concentration dependence and the presence of a single species or a single conformational ensemble in solution. The SAXS curve generated by averaging individual curves throughout the elution peak for scattering vectors (Q) ranging from 0.05 to 3.0 nm^{-1} (**Figure 6C**) yielded a molecular mass of 10.2 ± 0.8 kDa from the scattered intensity extrapolated at zero angle (I_0/C), confirming its monomeric state. The R_g value of 1.7 ± 0.1 nm determined by using the Guinier approximation at low Q values, was larger than that calculated from the crystal structure (1.3 nm). However, when the parts missing in the crystal structure, *i.e.* the flexible loop connecting N_{TAIL} to P_{XD} and both N- and C-terminal extensions, were incorporated into the structural model using the program CORAL (**Figure 6D**), the theoretical curve reproduced the experimental SAXS curve (χ = 1.5) (**Figure 6C**) supporting a structural model in which N_{TAIL} is bound to P_{XD} as in the crystal form. In conclusion, the interaction of N_{TAIL} with P_{XD} prevents the dimerization of P_{XD}, stabilizes the 3H bundle form and prevents the unfolding of helix α_3.

NiV P_{XD} conformational exchanges regulate virus replication

Among the different forms of P_{XD} that coexist and dynamically exchange in solution, only the monomeric 3H bundle is competent for interacting with N_{TAIL}. Assuming that similar conformational exchanges occur in the full-length protein, we hypothesized that within a single P tetramer the four P_{XD} domains exist in equilibrium between binding competent (3H) and incompetent conformers (2H and $2H_{DIM}$). In isolated NiV P_{XD}, this equilibrium is controlled by protein concentration, while in P_{FL} the effective concentration of P_{XD} must be increased because four P_{XD} molecules are intramolecularly connected to each other. Partial unfolding and dimerization of P_{XD} could represent a regulatory mechanism of the interaction between P and N and thus of the polymerase activities.

To test whether the dimerization of NiV P_{XD} influenced polymerase activity, we constructed a mutated NiV P gene, in which we replaced residues 655 to 709 by the corresponding residues of HeV (**Figure 7A**). Then, we used a reverse genetic system [8] to generate recombinant $rNiV_{HeV\text{-}PX}$ harboring the chimeric P gene instead of the parental counterpart and compared the ability of recombinant WT virus ($rNiV_{WT}$) and $rNiV_{HeV\text{-}PX}$ to replicate using two different cell lines. The modified NiV P gene included 12 mutations in P_{XD}, only one of which (Ile697Val) affected a residue directly involved in a hydrophobic interaction with N_{TAIL} (**Figure 1B**). Since all residues in N_{TAIL} that are involved in interaction with P_{XD} were conserved between NiV and HeV P (**Figure 2A**), and that the replacement of Ile697 by a valine cannot be suspected to affect the complex in a foreseeable way, we expected that differences in viral growth would mainly result from changes in P_{XD} conformational distribution, and in particular from the suppression of dimerization.

Vero E6 or 293T cells were infected at the same multiplicity of infection (MOI) of 0.01 either with $rNiV_{WT}$ or $rNiV_{HeV\text{-}PX}$. Viral titers were measured by $TCID_{50}$ (Median Tissue Culture Infectious Dose) assays and the amounts of genome copies were measured by RT-qPCR (Real-Time quantitative Polymerase Chain Reaction) at 48 and 54 hours post-infection (**Figure 7B and 7C**). The viruses replicated comparably well in both cell lines, while $rNiV_{HeV\text{-}PX}$ appeared to be slightly attenuated as also observed in western blot analysis of viruses released into the culture medium (**Figure 7D**). Attenuation of $rNiV_{HeV\text{-}PX}$ was further confirmed via northern blot analysis of virus specific mRNAs (N, P, M and F genes) synthesized in infected cells at 48h post infection (**Figure 7E**).

In conclusion, the substitution of NiV P_{XD} for HeV P_{XD} resulted in some degree of attenuation in virus-specific RNA synthesis, while with rather little effect on virus replication in cells.

A statistical dynamical model of the interaction between P and the nucleocapsid

The binding of multivalent ligands (tetrameric P protein) onto a linear lattice of potential binding sites (N_{TAIL} in linear nucleocapsid) is an inherently complex process, which depends on multiple parameters (e.g. McGhee 1974), and the conformational diversity of the ligand

(multiple forms of P_{XD} and high flexibility of full-length P) should add even more complexity. Our aims here was not to build a model that reproduce all the details and intricacies of the interactions between full-length tetrameric NiV P and the long helical NC, but to develop simple statistical dynamical models that predict some effects of the multimerization of full-length P and of the partial unfolding and dimerization of P_{XD} on NC binding. A brief description of the models including equations and some hypothesis and limitations are provided in the Supplementary Material.

The interaction between monomeric N_{TAIL} and P_{XD} of different paramyxoviruses is weak, with a dissociation constant in the micromolar range [23,53,57,69,70], but full-length P forms tetramers, supplying four anchoring feet to each P molecule. In a first simulation, we generated the binding curve for the association of monomeric P with one N_{TAIL} assuming a dissociation constant of 1 µM, and we tested the effect of adding up to three (leading to dimeric, trimeric or tetrameric P) additional intramolecular N_{TAIL}/P_{XD} interactions on the avidity of full-length P for a lattice of N molecules. Each additional intramolecular interaction with an adjacent N_{TAIL} was characterized by unimolecular equilibrium constant, K_{INTRA}, and for the sake of simplicity, we assigned identical values to K_{INTRA} for the association of the second, third or fourth P_{XD} (no cooperativity effect). Accounting for the different possible substates (n_j), we calculated the fraction of free P, which was the only substate where P was fully dissociated from the N lattice. In all other substates, P remained attached to the N lattice by at least one "foot" (**Supplemental Figure 5**). **Figure 8A** shows that even with a value of K_{INTRA} = 1, which means that the additional interaction provided no additional thermodynamic stability (ΔG_{INTRA} = 0 kJ.mol^{-1}), the binding curve shifted to a lower concentration range with increasing oligomerization state of P. This increase in binding avidity of P for the N lattice could be explained by the entropic effect associated with substate degeneracy. In our model, we obtained an apparent dissociation constant of 67 nM for tetrameric P (**Figure 8B**). Additional enthalpic contributions would enhance this avidity effect. The slope of the binding curve was unchanged because no cooperativity was implemented in the association of P_{XD} (**Figure 8A**).

In a second simulation, we considered tetrameric P and tested the effect of the partial unfolding of P_{XD} in the absence of dimerization, mimicking the situation encountered with the HeV proteins (**Supplemental Figure 6**). In agreement with our observations, we assumed that the partially unfolded P_{XD} could not bind to N_{TAIL}. The unfolding reaction was characterized by the equilibrium constant K_{UNFOLD}, and again for the sake of simplicity, we assigned identical values to all unfolding/folding steps in the model. In this case, the occurrence of partial unfolding reduced the avidity of P for the N lattice in a manner dependent on the value of K_{UNFOLD} (**Figures 8C and 8D**). Again, the slope of the binding curve is not affected since no cooperativity was introduced into the model.

In a third simulation, we also considered tetrameric P and tested the effect of partial unfolding of P_{XD} combined with the dimerization of the partially unfolded form, mimicking the situation

encountered with the NiV proteins (**Supplemental Figure 7**). We considered only the case where dimerization occurred intramolecularly, either within free tetrameric P or within tetrameric P bound to the N lattice. The dimerization was thus characterized by unimolecular equilibrium constant (K_{DIMER}). This additional feature affected the unbound state of P as well as the states where only one or two P_{XD} were bound to the N lattice. In this case, the multiplicity of the different substates of free and bound P also led to a decrease in avidity depending on the value of K_{DIMER} (**Figures 8E and 8F**).

Discussion

Thermodynamic stability controls the conformational diversity of paramyxovirus P_{XD} in solution

The presence of the small helical X domain (P_{XD}) at the C-terminal end is a common feature of all paramyxovirus phosphoproteins. In their isolated form in solution near 20°C, the P_{XD} from different *Paramyxoviridae* exhibits a wide spectrum of dynamical behaviors, ranging from fully folded (measles virus, MeV), to partially folded (mumps virus, MuV; NiV) or mainly unfolded (Mapuera virus), mirroring their intrinsic thermodynamic stability. This conformational diversity in solution was nicely exemplified in a comparative study of P_{XD} from different members of the genus Rubulavirus, which clearly had different thermodynamic stabilities [46,48]. For their part, P_{XD} of MeV (genus Morbillivirus) and Sendai virus (SeV) (Respirovirus) appeared to be well folded and stable near 20°C as demonstrated by NMR spectroscopy ([23,47,71]. Also, the size of MeV P_{XD} was insensitive to the addition of trimethylamine N-oxide (TMAO), an osmolyte that promotes the folded structure of proteins [72], in contrast to that of MuV [46], even if equilibrium and kinetic folding intermediates were observed within the urea-induced unfolding transition [73].

With regards to NiV and HeV P_{XD}, both domains crystallized and their NMR spectra showed line widths and chemical shift dispersion typical of folded domains ([23] and this paper), but others and we found evidence that both domains populated partially folded forms in solution at 20°C: (i) At low concentration in solution, the hydrodynamic radius (R_h) of both P_{XD} determined by SEC was larger than that of RNAse A and thus larger than expected for a compact globular domains of ~6.3 kDa (**Figure 3A**). Previously, the size of the HeV domain was shown to be controlled by surface charges [58]. (ii) The radii of gyration (R_g) measured by SAXS extrapolated at zero concentration were also larger than those calculated with CRYSOL for the 3H bundle conformation extracted from crystal structures (**Figure 4**). (iii) By NMR spectroscopy, we demonstrated the co-existence of a minor form of NiV P_{XD}, in which helix α_3 was dissociated from the hairpin made of helix α_1 and α_2 (**Figures 3C-F**). (iv) Considering the midpoint of the transition as a crude measurement of thermodynamic stability (assuming $\Delta C_P = 0$) NiV P_{XD} appeared marginally stable (Tm = 42.5 °C), on the verge of its global unfolding at 20°C, whereas HeV P_{XD} was more stable (Tm = 53.5 °C) (**Figure 3G**). This difference in stability was unexpected given the small size of the domains and the conservative modifications between NiV and HeV sequences.

In addition, we found evidence for a concentration-dependent equilibrium of NiV P_{XD} between monomeric and dimeric forms, but not for HeV P_{XD}. (i) The hydrodynamic radius and the radius of gyration of NiV P_{XD} increased with protein concentration, while the intensity of scattered light or X-ray revealed a molecular mass increase with protein concentration (**Figure 4**). (ii) Again, for NiV P_{XD} but not for HeV P_{XD}, dimeric forms were selected in the ensemble models that fitted the SAXS data (**Figure 5**). The dimeric form of NiV P_{XD} was not detected by NMR spectroscopy, possibly because of its larger correlation time (**Figure 1F**). However, if we accounted for only the monomeric species, a good

correlation was found between the fractions of the 3H bundle (90%) and monomeric 2H hairpin (10%) forms determined in the NMR CEST experiment (90%/10%) (**Figure 3F**) and by ensemble modeling using the SAXS data (93%/7%) at a similar protein concentration (8 $mg.mL^{-1}$). Regarding the physiological relevance of the dimeric 2H hairpin conformation, it should be noted that all *Paramyxoviridae* P proteins form multimers. This should increase the effective concentration of P_{XD}, thereby favoring dimer formation within the multimer. Because both domains eluted in a single chromatographic peak, we inferred that the exchange time between the different forms is shorter than the chromatographic time.

In conclusion, different accessible conformational states of NiV and HeV P_{XD} coexist in solution (Figure 9) and their relative populations depend on their intrinsic thermodynamic stability. More generally, near room temperature, the folded state of some P_{XD} dominates (e.g. MeV), whereas for others the folded state coexists with partially unfolded states (e.g. NiV, MuV), and in some cases, the folded state is very lowly populated (e.g. Mapuera virus). As we have demonstrated with our statistical-dynamical model, playing on the thermodynamic stability of P_{XD} is an efficient way for the virus to control the strength of the interactions between P and N, and the high mutation rate in these viruses provides a way to readily modify the amino acid sequence and adapt the thermodynamic stability of this protein domain. We can also hypothesize that changing the binding affinity of P for N could affect the rate of the polymerase and thus could allow the virus to adapt its growth to infect its host in an optimal way (see below).

Conformational diversity of atomic resolution structures

The high-resolution structure of unbound P_{XD} has been solved for seven viruses belonging to four genera by X-ray crystallography (MeV, HeV, NiV, MuV, hPIV4b, MenV) or NMR spectroscopy (SeV) [23,46–48,74]. In crystals, MeV, HeV and MuV P_{XD} adopted a 3H bundle fold, commonly referred as the canonical fold [23,46,50]. Similarly, Menangle virus P_{XD} in fusion with MBP adopted the same fold [48] and SeV P_{XD} was shown to have a 3H fold by NMR spectroscopy [47]. By contrast, NiV P_{XD} and hPIV4b P_{XD}, the latter in fusion with MBP, formed dimeric 2H hairpins in crystals [48]. The structure of NiV P_{XD} comprised a short helix (α_1) and a long one ($\alpha_{2\text{-}3}$), and it formed dimers by burying the face of the α_1-α_2 hairpin that binds α_3 in the 3H conformation. The structure of hPIV4b P_{XD} comprised two short helices also corresponding to helices α_1 and α_2 of the canonical conformation and was very similar to the 2H core of NiV P_{XD}, while the C-terminal end corresponding to the third helix was not visible and thus likely flexible [48]. As in NiV $P_{XD,}$ the third α-helix could not pack on α_1 and α_2 as this surface was used for the dimerization. In NiV P_{XD}, the presence of a network of salt-bridges and H-bonds (**Figure 1E**) and crystal contacts (Supplementary figures 2 B-C) likely explain the extension of the helix α_2 by stabilizing one additional turn at the C-terminal end of helix α_2 and thereby the presence of sub-populations of 2H hairpin and 2H dimers in solution. The presence of dimers in solution could explain that this protein formed dimers in crystal, where the long helix was stabilized by crystal contacts. In HeV P_{XD}, all residues involved in this network of polar interactions are conserved except for the

conservative modifications of residues R661 (K659 in HeV) and K665 (R663 in HeV). Although seemingly insignificant, these changes could explain the absence of formation of this polar interaction network in HeV P_{XD} and the absence of dimers [23].

The structure of the complex between P_{XD} and N has also been characterized by X-ray crystallography, NMR spectroscopy or cryo-electron microscopy for different viruses belonging to different genera of *Paramyxoviridae* (MeV, Morbillivirus; NiV and HeV, Henipavirus; SeV, Respirovirus) ([21,23,53,57,75] and this study), whereas that between P_{XD} and L has been recently obtained for parainfluenza virus 5 (PIV5) (genus Rubullavirus) by cryo-electron microscopy [44]. In both complexes, P_{XD} adopted the canonical 3H bundle form, where each face of the triangular prism interacted with a different partner [41]. The face created by helices α_2 and α_3 bound a helical segment of N originating in either a α-MoRE of the intrinsically disordered N_{TAIL} region [21,23,53,57] or a folded helix of N_{CORE} (MuV, Rubullavirus) [75]. The face created by helices α_1 and α_3 bound the polymerase (PIV5, Rubullavirus) [40,44,45], whereas the last face (α_1 and α_2) interacted with N_{CORE} in a way that is not yet fully understood (CDV, Morbillivirus) [41]. For NiV, the N_{TAIL}-P_{XD} interaction has been documented in several studies, including the mapping of the P binding region in N_{TAIL} [22,37,57]. Here, we report that in the crystal, NiV P_{XD} also adopted the canonical 3H bundle form when bound with the α-MoRE of N_{TAIL}. Residues 473-489 of N_{TAIL} formed a regular helix that docked on the surface formed by helices α_2 and α_3. In this complex, all residues involved in both interfaces were conserved between NiV and HeV (**Fig. 1B and 2A**), rationalizing the cross-species interactions reported previously [22], while many of these residues were also conserved throughout the Henipaviruses suggesting a common mode of binding (**Supplemental Figure 1**).

The crystal structure of the NiV P_{XD}-N_{TAIL} complex can be compared to that of MeV [21], and to models available for MeV, NiV and HeV [50,57,58]. Besides the coupled folding-upon-binding mechanism that is common to MeV and other viruses and a similar 4-helix bundle fold, the complex of NiV presented a striking difference with that of MeV; NiV N_{TAIL} was antiparallel with helix α_3, whereas MeV N_{TAIL} was parallel to helix α_3 [21]. In both cases, the structure was obtained by fusing N_{TAIL} to the C-terminal end of P_{XD} through a nine amino acid linker. The length of the linker was deemed sufficient to allow a helical N_{TAIL} to bind either parallel or antiparallel with respect to helix α_3 [21]. In the MeV crystal, N_{TAIL} was swapped between different molecules, whereas, in the NiV crystal, N_{TAIL} was bound intramolecularly to P_{XD}. The formation of a network of H-bond between P_{XD} and N_{TAIL} in the antiparallel arrangement provided some relevance to our structure (**Figure 2F**). The side-chain atoms involved in these interactions (E680 and D703 in P_{XD} and R480 and S475 in N_{TAIL}) are strictly conserved within Henipavirus (**Supplemental Figure 1**). However, in the case of NiV, *a posteriori* analysis of the crystal structure revealed that the nine amino acid linker would require some fraying of the C-terminal end of helix α_3 for allowing the opposite arrangement of N_{TAIL}. Also, we cannot exclude a model where in the highly dynamical complex between P and the nucleocapsid, both orientations could exist depending on

stochastic encounters between these two proteins. It is worth noting that models with both orientations of N_{TAIL} on the P_{XD} surface were generated with equal probability from NMR data obtained for the HeV N_{TAIL}-P_{XD} complex [23] but that a parallel orientation was proposed for this complex on the basis of site-directed mutagenesis [58]. In the MeV complex, side-chain atoms of Asp493 in P_{XD} form H-bond with Ser491 in N_{TAIL} [21], and similar residues are conserved at these positions within the genus Morbillivirus, thus providing relevance to the parallel arrangement.

The roles of the interaction between N_{TAIL} and P_{XD}

For a long time, the only assigned function of P_{XD} was to connect P, and thereby the L polymerase, to the nucleocapsid (NC) through a direct interaction with N. Past and recent studies revealed additional interactions with L and more intricate functions within the transcription/replication complex [34,40,41,44,45,76]. Although we cannot exclude that the large variability in thermodynamic stability of P_{XD} throughout the family *Paramyxoviridae* is inherent to its small size, it is however tempting to consider it as an adaptive capacity through the modulation of the interaction with the NC. Two hypotheses can then be considered regarding the potential effect of partial unfolding of NiV and HeV P_{XD} and/or dimerization of NiV P_{XD} on the interaction with N_{TAIL}.

A first hypothesis is that the conformation diversity of P_{XD} regulates the activity of the polymerase by controlling its motion along the NC. A model for the operation of this molecular machine involves that by cartwheeling or crawling along the nucleocapsid template, P maintains the connection between the nucleocapsid and the polymerase when the latter moves along the template RNA and thus avoids premature termination of RNA synthesis [77,78]. NiV P is tetrameric and even if the affinity measured for a single P_{XD} is low (>1 μM) [58], the statistical-dynamical model clearly demonstrated that tetrameric P can bind with an overall strong affinity to the nucleocapsid (**Figure 8**). Polymerase is the molecular motor that moves along the RNA template as it synthesizes RNA and it carries P with it during this process. A mechanism, where each P_{XD} alternatively dissociates from N_{TAIL} and re-associates with the N_{TAIL} of another N subunit downstream along the nucleocapsid, allows P to move along the nucleocapsid while remaining constantly bound to it. In this way, a strong interaction between P_{XD} and N_{TAIL} would act as a break on the polymerase complex, whereas weak interaction would ease up the motion. A correlation has been observed experimentally between the strength of P_{XD}/N_{TAIL} interaction and polymerase activity suggesting that, indeed, this interaction controls the motion of the polymerase complex along its template and thus controls polymerase activities [39,79]. The discoveries that isolated NiV and HeV P_{XD} exhibited conformational heterogeneity and that some populated conformations were non-competent for binding N_{TAIL} (Figure 9), suggested a possible role for the conformational diversity of P_{XD} in modulating the attachment of P to the nucleocapsid and thus in regulating polymerase activity. In the same way, the findings that NiV P_{XD} can dimerize, whereas HeV P_{XD} cannot, suggested that the N_{TAIL}/P_{XD} interactions could control

differently the polymerase activity in these viruses. Our simulations showed that partial unfolding of P_{XD} or dimerization of P_{XD} could decrease the affinity of P_{XD} for N_{TAIL} (**Figures 8 and 9**). Indeed, the N_{TAIL} binding site is only present in the monomeric 3H bundle conformation of P_{XD}, and is absent in both the monomeric 2H conformation and in the dimeric form. The dimerization of P_{XD} should thus reduce its apparent binding affinity for N_{TAIL} and thereby allow the polymerase to move more readily along its template. The other way round, abrogating the dimerization of P_{XD} could create an impediment to the motion of the polymerase and correlatively reduce its activity. The results obtained with the chimeric NiV virus in which we exchanged the w.t. P_{XD} sequence with the HeV P_{XD} sequence ($rNiV_{HeV\text{-}PX}$) showed no major difference in virus replication in comparison with the parental virus but some attenuation apparently caused by a delay in mRNA synthesis followed by lower expression of viral protein and virus release. As the sequence of the interacting region in N_{TAIL} is strictly conserved between the two viruses, the difference in behavior can potentially be attributed to P_{XD}, (even if we cannot exclude specific interactions between a upstream region of P and N_{TAIL} - [58]). It seems thus plausible that NiV, in comparison with HeV, through formation of P_{XD} dimers possesses an additional mechanism to further modulate the interaction of P with NC and thereby fine-tune mRNA and protein production. At this stage, we have no indication of the advantage that such regulation can bring to the virus, but we can hypothesize that it allows the virus to grow under different external conditions, e.g. different temperatures. In this prospect, the next step would be to investigate whether the dimerization of P_{XD} is related to the ability of NiV to adapt to different hosts more easily than HeV.

A second hypothesis is that the partial unfolding and/or dimerization of P_{XD} control the fraction of P that is not bound to NC. In the protein expression gradient resulting from the STOP-START mechanism of the polymerase complex, more P protein is produced than required to form L-P_4 complexes. In addition to acting as a hub within the replication complex, P performs other functions that do not require an anchoring to the nucleocapsid, for instance the interactions with STAT1 and STAT2 to counteract the innate immune system [12]. The partial unfolding or dimerization of P_{XD} could modulate the fraction of free P, which could then diffuse in the cytoplasm or in the nucleus. In the proposed statistical dynamics model, at a particular concentration of P, e.g. at a concentration of P of 1.0 micromolar, the fraction of free P (completely released from the nucleocapsid) increased by about 10% when dimerization (K_{DIMER} = 1) was introduced by comparison with the situation in its absence. This seemingly minor change in binding affinity produced a sizeable increase of the fraction of free P. Such changes in the population of free P could have some impact on the interactions with cellular partners.

In conclusion, our results unveiled a mechanism in which the conformational stability of P_{XD}, can control the interactions of P with the nucleocapsid and the fraction of P available for interacting with cellular partners.

Material and methods

Multiple sequence alignments

Multiple sequences alignments were performed with Clustal omega [80], and rendering was done with ESPript 3 [81]. The UniProt [82] accession numbers of the sequences of Henipavirus P and N used and the abbreviations of species names are as follows: Phosphoprotein - Nipah virus (NiV - Q9IK91), Hendra virus (HeV - O55778), Cedar virus (CedV - J7GXK5), Ghanaian bat paramyxovirus (GhV - I0E089). Nucleoprotein: NiV - Q9IK92), HeV - O89339), CedV - J7H328, GhV - I0E088.

Protein expression and purification.

Nipah virus P_{XD} (residues 655-709, Uniprot Q9IK91) and Hendra virus P_{XD} (residues 653-707, Uniprot O55778) were cloned in pET28 or pETM40 vectors with a C-terminal 6His tag or a TEV cleavable N-terminal maltose binding protein (MBP) tag, respectively. NiV P_{XD}-N_{TAIL} fusion protein was cloned in pET28 vector. All proteins were expressed in *E. coli* BL21 (DE3) Rosetta cells. Cells were grown at 18 °C in LB medium until O.D. reached 0.6-0.8, and protein expression was induced overnight at 20°C by addition of isopropyl-β-D-thiogalactoside (IPTG) to a final concentration of 1 mM. Cells were harvested and the pellet was suspended in buffer A (20 mM Tris-HCl buffer at pH 7.5 containing 150 mM NaCl). All buffers were supplemented with Complete protease inhibitor cocktail (Roche). Cells were disrupted by sonication, and the crude extract was cleared by centrifugation at 45,000 g at 4°C for 20 min. For 6His tagged proteins, the supernatant was loaded on Ni-NTA resin (QIAGEN), equilibrated in buffer A. The column was washed with 10 column volumes of buffer A containing 20 mM imidazole (Sigma), and the protein was eluted with buffer A containing 300 mM imidazole. For MBP tagged proteins, the supernatant was loaded onto an amylose resin (New England Biolabs) equilibrated in buffer A. The column was washed with 10 column volumes of buffer A containing 500 mM NaCl, and the protein was eluted with 50 mM maltose (Sigma) in buffer A. MBP-P_{XD} fusions were subsequently cleaved with TEV protease to remove the MBP tag. The protease was added at an approximate weight ratio of 100:1 (fusion protein:TEV), and digestion was performed overnight in buffer A at 4 °C. After concentration with Vivaspin concentrators (Sartorius) of 3 kDa cut-off, protein solutions were loaded onto a Superdex 75 (S75) column (GE Healthcare) equilibrated in buffer A at 4°C.

SEC-MALLS experiments

Size exclusion chromatography (SEC) combined with on-line detection by multi-angle laser light scattering (MALLS) and refractometry (RI) is a method for measuring the absolute molecular mass of a particle in solution that is independent of its dimensions and shape [83]. SEC was performed with a S75 column or a S200 column (GE Healthcare) equilibrated with 20 mM Tris-HCl buffer containing 150 mM NaCl. Separations were performed at 20 °C with a flow rate of 0.5 $mL.min^{-1}$. On-line multi-angle laser light scattering (MALLS) detection was performed with a DAWN-HELEOS II detector (Wyatt Technology Corp.) using a laser emitting at 690 nm, and protein concentration was measured on-line by differential refractive

index measurements using an Optilab T-rEX detector (Wyatt Technology Corp.) and a refractive index increment, *dn/dc*, of 0.185 mL.g^{-1}. Weight-averaged molar masses (Mw) were calculated using the ASTRA software (Wyatt Technology Corp.). For size determination, the column was calibrated with proteins of known Stokes radius (R_S) [84].

Circular dichroism spectroscopy

CD experiments were performed on a JASCO model J-810 CD spectropolarimeter equipped with a Peltier temperature controller. Far UV CD spectra were recorded at 20°C. NiV and HeV P_{XD} were at a final concentration of 20 µM in 10 mM sodium phosphate buffer at pH 7.5 containing 150 mM NaCl and measurements were made in 1 mm optical length cuvette. After subtracting the blank signal, the CD signal was converted to mean molar residue ellipticity (in deg.cm^{-2}.dmol^{-1}) and helix content was estimated as described previously [18]. The thermal denaturation curves were fitted assuming a two state model as described [85]:

$$U \underset{}{\overset{K}{\rightleftharpoons}} N$$

where U represents the unfolded form and N the folded form. The equilibrium constant for unfolding is defines as:

$$K = \frac{[U]}{[N]}$$

The variation of molar ellipticity at 222 nm is then fitted with the equation:

$$-[\Theta]_{222nm} = \frac{([\Theta]_N + m_N T) + [\Theta]_U \, exp\left(\frac{-\Delta G^0}{RT}\right)}{1 + exp\left(\frac{-\Delta G^0}{RT}\right)} \qquad \text{(Eq. 1)}$$

where the baseline for N is modeled by a line with intercept $[\Theta]_N$ and slope m_N to account for the small changes in signal at low temperature and the baseline for U is modeled by a horizontal line ($[\Theta]_U$). Given the small temperature range sampled and the small size of the protein domain, our data were not sufficient for a precise determination of ΔC_P, we chose a simple approach in which we assume that $\Delta C_P = 0$ and defined the free energy difference by:

$$\Delta G^0 = \Delta H^0 \left(\frac{1-T}{1-T_m}\right) \qquad \text{(Eq. 2)}$$

Small angle X-ray scattering experiments

Small angle X-ray scattering (SAXS) data were collected at the BioSAXS beamline (BM29) of the ESRF (http:// www.esrf.eu/UsersAndScience/Experiments/MX/About_our_beamlines /BM29). Data processing and *ab initio* modeling was performed with the ATSAS package [86]. The forward scattering intensity was normalized with bovine serum albumin and lysozyme as reference proteins as previously described [87]. The scattering from the buffer was measured before and after each sample measurement and was used for background subtraction using the program PRIMUS. Scattering data were collected at different

concentration. R_g was estimated at low Q values for which $Q.R_g < 1.3$ using the Guinier approximation.

SAXS data analysis was performed using CORAL from the ATSAS package [86]. A model based on the crystal structure of the chimeric P_{XD}-N_{TAIL} complex was created, where N-the linker and the N- and C-terminal ends were represented as random polypeptide chains.

Ensembles of physically accessible P_{XD} conformers were generated with the program RANCH [66], while ensemble selection was performed with the program EOM [66].

Monomer-dimer equilibrium

To model the experimental forward scattered intensity as a function of the total concentration protein expressed in weight per unit volume (C_T), we used the approach previously described [89]. Briefly, for monomer-dimer equilibrium, the extrapolated intensity at zero angle, I_0, divided by concentration, I_0/C_T, is the sum of forward scattered intensity values for monomer ($I_{mono}(0)$) and dimer ($I_{dim}(0)$) weighted by the weight fractions for the monomer, f_{mono}, and dimer, f_{dim}.

$$\frac{I_0}{C} = f_{mono}.I_{mono}(0) + f_{dim}.I_{dim}(0) \qquad \text{(Eq. 3)}$$

The dissociation constant is given by:

$$K_D = \frac{[mono]^2}{[dim]} = \frac{2.f_{mono}.C_T}{M_{mono}.(1-f_{mono})} \qquad \text{(Eq. 4)}$$

where [mono] and [dim] are the molar concentrations of the monomer and dimer, respectively, and M_{mono} is the molecular mass of the monomer. The fraction of the monomer is given by the following equation [89]:

$$f_{mono} = -K_D.M_{mono} + \frac{\sqrt{K_D^2.M_{Mono}^2 + 8.C_T.K_D.M_{mono}}}{4.C_T} \qquad \text{(Eq. 5)}$$

Because $f_{mono} + f_{dim} = 1$ and $I_{dim}(0) = 2\ I_{mono}(0)$, we can write:

$$\frac{I_0}{C_T} = M_{mono}\ (2 - f_{mono}) \qquad \text{(Eq. 6)}$$

where f_{mono} is given by equation 5.

Crystallography

Initial crystallization conditions for the NiV P_{XD} and N_{TAIL}-P_{XD} fusion were identified at the High Throughput Crystallization Laboratory of the EMBL Grenoble Outstation (https://htxlab.embl.fr). Crystals of NiV P_{XD} were obtained by the hanging-drop vapor diffusion technique in 0.1 M bis-Tris/HCl buffer at pH 6.0 containing 25% PEG 3350 and 0.2 M magnesium chloride at 20 °C. Crystals were harvested from the drop, briefly soaked in the reservoir solution supplemented with 20% glycerol and flash frozen in liquid nitrogen before data collection. X-ray diffraction data for the native NiV P_{XD} were collected at the ID29

beamline of the ESRF at a wavelength of 0.9793 Å, those for the NaI soaked NiV P_{XD} at beamline ID29 of ESRF and those for the NiV N_{TAIL}-P_{XD} fusion at beamline ID14-4 of the ESRF. NaI soaked NiV P_{XD} diffraction data were collected using an inverse beam strategy. All data were collected at a temperature of 100 K and were processed with the XDS and merged with XSCALE and formats converted with XDSCONV [90]. Initial phases for NiV P_{XD} were obtained by the SIRAS method using anomalous scattering from iodine atoms with the program HKL2MAP [91]. A model was initially constructed with the Buccaneer program [92] from the CCP4 suite [93] using the dataset obtained with NaI soaked crystals. Subsequently, phases were refined for the native dataset at higher resolution with the phenix.refine program using isotropic atomic ADPs and TLS refinement [94] and after visual inspection using Coot [95]. Due to the high symmetry and low atom content of the unit cell, relatively few (~4500) unique reflections were available for refinement. Different strategies using different number of reflections corresponding to 5%, 10% or 15% of total reflections were used for cross-validation, leading to slightly different final R/Rfree values but with virtually no difference in the final electron density or model coordinates. Crystals of NiV N_{TAIL}-P_{XD} fusion protein were obtained by the hanging-drop vapor diffusion technique in 0.1 M sodium acetate buffer at pH 4 containing 20% PEG 550. Crystals were harvested from the drop, briefly soaked in the reservoir solution supplemented with 20% glycerol and flash frozen in liquid nitrogen before data collection. Initial phases for NiV N_{TAIL}-P_{XD} fusion protein were obtained by molecular replacement using models generated by the program Rosetta [60]. A model was initially constructed with the Ample program from the CCP4 suite [61] and subsequently refined using Refmac5 [96] and Coot [95]. The quality of all final models was checked with MolProbity [97].

NMR spectroscopy

The backbone spectral assignment of NiV P_{XD} was carried out using a 1.3 mM ^{15}N, ^{13}C labeled sample in 20 mM HEPES, pH 6.0 and 500 mM NaCl. A set of six BEST-type triple resonance experiments correlating $^{13}C'$, $^{13}C\alpha$ and $^{13}C\beta$ frequencies (ref: https://www.ncbi.nlm.nih.gov/pubmed/17468025) were acquired at 25°C on an 600 MHz Agilent spectrometer equipped with a room-temperature probe. Spectra were processed using NMRPipe [98] and analyzed using CcpNmr [99] or SPARKY [100]. Sequential connectivities were obtained using Nexus under CcpNmr followed by manual verification of the assignments. Secondary structure propensities (SSP) of NiV P_{XD} were calculated from the experimental $C\alpha$ and $C\beta$ chemical shifts using the SSP algorithm [63].

^{15}N chemical exchange saturation transfer (CEST) was carried out at a ^{1}H frequency of 600 MHz at 25°C on a 8.2 mg/mL (1,300 μM) sample of NiV P_{XD} in 20 mM Tris/HCl, pH 7.5 and 150 mM NaCl. The spectral assignment was transferred to these conditions by recording ^{1}H-^{15}N HSQC spectra at intermediate pH and salt conditions. An ^{15}N B_1 field strength of 20 Hz was applied during a constant period of 300 ms for the CEST experiment. Data from several residues displaying significant chemical shift differences between the ground and excited states and isolated resonances in the NMR spectra were analyzed simultaneously according to a two-site exchange model using the program ChemEx [64]. ^{15}N random coil chemical shift values for comparison with the CEST-derived chemical shift differences were taken from

ncIDP [65].

Cells and Viruses

Vero E6, HEK 293T and BSR T7/5 cells were cultured as described in [8]. The recombinant NiV (rNiV) is based on genomic sequence of NiV isolate from Malaysia (GenBank accession N° AY029767). All experiments with infectious NiV were performed at Jean Mérieux INSERM BSL4 Laboratory in Lyon, France.

Rescue of recombinant NiVs

A cDNA encoding P protein of NiV, in which residues 655-709 were replaced by the corresponding residues of HeV, was constructed through deletion mutagenesis and PCR cloning. Two plasmids containing the full-length NiV genome with either wild type P gene sequence (pFL-NiV_{WT}) or harbouring the chimeric NiV-HeV P gene (pFL-$NiV_{HeV\text{-}PXD}$) were used to generate recombinant viruses as previously described [8]. Supernatants from successful rescue experiments were used to generate viral stocks in Vero E6 cells. Virus titers were estimated by 50% tissue culture infective dose (TCID50) assay on Vero E6 cells. Presence of introduced mutations and absence of any other substitutions in L, P and N genes were confirmed by Sanger sequencing of viral RNA.

Virus growth experiments.

Vero E6 and HEK 293T cells were infected with viruses at a multiplicity of infection (MOI) of 0.01, as described previously [13]. Culture supernatants were harvested at 24, 30, 48, 54 and 72 hours post-infection and subjected to Western blot and RT-qPCR analyses. Two step RT-qPCR was performed essentially as described in [101]. Briefly, cDNA synthesis was made on viral RNA isolated from culture supernatants using N-forward primer 5'-GGCAGGATTCTTCGCAACCATC and SuperScriptIII reverse Transcriptase (Invitrogen). After inactivation of RT at 65° for 10 min quantitative PCR was performed with N-forward and N-reverse primer 5'- GGCTCTTGGGCCAATTTCTCTG using EurobioGreen qPCR Mix Lo-Rox (Eurobio) according to manufacturer's recommendations and the following protocol: denaturation at 95° C for 2 min, 45 cycles at 95° C for 5 s and 60° C for 30 s in Light Cycler 96 (Roche).

Viral titers were accessed by TCID50 protocol. Relative levels of gene expression were calculated as previously described [102]. Image Quant software TL Dv.8 (GE Healthcare) was used to determine levels of viral proteins in comparison with Mock control.

Northern blotting.

Total RNA from virus-infected cells was extracted using an RNeasy kit (Qiagen) according to the manufacturer's instructions. Equal amounts of RNA were separated on 1% agarose gel and were transferred onto a Biodyne B membrane using vacuum blotter (Bio-Rad). Biotin-labeled DNA probes targeting the N, P, M or F genes in ULTRAhyb-Oligo Hybridization buffer (Invitrogen) were used for overnight hybridization at 42°C. NiV specific mRNA were visualized using alkaline phosphatase coupled streptavidin detection system according to the

manufacturer's protocols (KPL). RNA bands were quantified using Image Quant software TL D v8 (GE Healthcare) and then normalized to cellular 28S ribosomal mRNA.

Biotinylated DNA probes (200-300bp) were generated by PCR in the presence of 40% Biotin-16-UTP using plasmid containing NiV full length genome and the following pairs of primers for N, P, M and F gene, respectively: 5'-GGAAGGCTTGATGAGAATCCTC and 5'-ACGTATTTAGCCCATCTTCTAG; 5'-ACTTCAAGCCCTGAGAGAGG and 5'-GCTAGTCTGAGGGCCAACG; 5'-AATTGCTGCCTACCCTCTGG and 5'-TTCGTGGAATCATGTAGATTCC; 5'-GGCAGGAGTTGCTATTGGGA and 5'-AGAGGTACTTTGATAATGCCA.

Author contributions

JMB, FY, VVE, MRJ, MB and MJ conceived the experiments; JMB, FY, GC, RS, FC, CD, CM, VVA, MF and MRJ performed the experiments; JMB, FY, GC, RS, VVA, MRJ, VVE, MB and MJ analyzed and interpreted the data; JMB, FY, VVE, MRJ, MB and MJ wrote the paper.

ACCESSION CODES

Coordinates and structure factors have been deposited in the Protein Data Bank under accession codes 7PNO and 7PON.

Acknowledgments

F.Y. was supported by a predoctoral fellowship from the Région Rhône-Alpes. We thank Philip Lawrence (Univ. Catholique de Lyon) for his help in setting up the initial rescue of mutant virus and Cédric Leyrat (IGF, Montpellier) for discussion and for reading the manuscript. The work was supported by grants from the French Agence Nationale de la Recherche to M.J. and M.B. (ANR BSV8-2012—NNViPol) and to M.J. and V.V. (ANR-18-CE11-0014-02), from the Fond de la Recherche Médicale (FRM) (grant "Equipe 2017" DEQ20170336754) to M.J. and from the FINOVI Fundation to M.J. and V.V. We acknowledge the European Synchrotron Radiation Facility for the allocation of beamtime on ID14-3 and ID23-1 and the Synchrotron SOLEIL for the allocation of beamtime on Proxima 1. This work used the platforms of the Grenoble Instruct-ERIC center (ISBG ; UAR3518

CNRS-CEA-UGA-EMBL) within the Grenoble Partnership for Structural Biology (PSB), supported by FRISBI (ANR-10-INBS-0005-02) and GRAL, financed within the University Grenoble Alpes graduate school (Ecoles Universitaires de Recherche) CBH-EUR-GS (ANR-17-EURE-0003). All experiments involving live NiVs were carried out in the INSERM Jean Merieux BSL4 laboratory in Lyon, France.

References

[1] Chua KB, Bellini WJ, Rota PA, Harcourt BH, Tamin A, Lam SK, et al. Nipah virus: a recently emergent deadly paramyxovirus. Science (80-) 2000;288:1432–5. doi:8529 [pii].

[2] Selvey LA, Wells RM, Mccormack JG, Ansford AJ, Murray K, Rogers RJ, et al. Infection of humans and horses by a newly described morbillivirus. Med J Aust 1995;162:642–5.

[3] Broder CC, Bishop KA. Hendra and Nipah Viruses: Lethal Zoonotic Paramyxoviruses. Emerg Infect 8 2008:155–87. doi:10.1128/9781555815592.ch9.

[4] Wong KT, Shieh WJ, Kumar S, Norain K, Abdullah W, Guarner J, et al. Nipah virus infection: pathology and pathogenesis of an emerging paramyxoviral zoonosis. Am J Pathol 2002;161:2153–67.

[5] Satterfield BA, Dawes BE, Milligan GN. Status of vaccine research and development of vaccines for Nipah virus. Vaccine 2016;34:2971–5.

[6] Luby SP. The pandemic potential of Nipah virus. Antiviral Res 2013;100:38–43. doi:10.1016/j.antiviral.2013.07.011.

[7] Halpin K, Bankamp B, Harcourt BH, Bellini WJ, Rota PA. Nipah virus conforms to the rule of six in a minigenome replication assay. J Gen Virol 2004;85:701–7.

[8] Ciancanelli MJ, Volchkova VA, Shaw ML, Volchkov VE, Basler CF. Nipah virus sequesters inactive STAT1 in the nucleus via a P gene-encoded mechanism. J Virol 2009;83:7828–41. doi:JVI.02610-08 [pii] 10.1128/JVI.02610-08.

[9] Gutsche I, Desfosses A, Effantin G, Ling WL, Haupt M, Ruigrok RWH, et al. Near-atomic cryo-EM structure of the helical measles virus nucleocapsid. Science (80-) 2015;348:704–8.

[10] Ker D-S, Jenkins HT, Greive SJ, Antson AA. CryoEM structure of the Nipah virus nucleocapsid assembly. BioRxiv 2020:2020.01.20.912261. doi:10.1101/2020.01.20.912261.

[11] Jordan PC, Liu C, Raynaud P, Lo MK, Spiropoulou CF, Symons JA, et al. Initiation, extension, and termination of RNA synthesis by a paramyxovirus polymerase. PLOS Pathog 2018;14:e1006889. doi:10.1371/journal.ppat.1006889.

[12] Jensen MR, Yabukarski F, Communie G, Condamine E, Mas C, Volchkova V, et al. Structural Description of the Nipah Virus Phosphoprotein and Its Interaction with STAT1. Biophys J 2020:1–19. doi:10.1016/j.bpj.2020.04.010.

[13] Yabukarski F, Lawrence P, Tarbouriech N, Bourhis JM, Delaforge E, Jensen MR, et al. Structure of Nipah virus unassembled nucleoprotein in complex with its viral chaperone. Nat Struct Mol Biol 2014;21:754–9. doi:10.1038/nsmb.2868.

[14] Kulkarni S, Volchkova V, Basler CF, Palese P, Volchkov VE, Shaw ML. Nipah virus edits its P gene at high frequency to express the V and W proteins. J Virol

2009;83:3982–7. doi:JVI.02599-08 [pii] 10.1128/JVI.02599-08.

[15] Yoneda M, Guillaume V, Sato H, Fujita K, Georges-Courbot MC, Ikeda F, et al. The nonstructural proteins of Nipah virus play a key role in pathogenicity in experimentally infected animals. PLoS One 2010;5:e12709. doi:10.1371/journal.pone.0012709.

[16] Jamin M, Yabukarski F. Non-segmented negative-sense RNA viruses – structural data brings new insights into nucleocapsid assembly. Adv Virus Res 2016;97:143–85.

[17] Jensen MR, Communie G, Ribeiro Jr. EA, Martinez N, Desfosses A, Salmon L, et al. Intrinsic disorder in measles virus nucleocapsids. Proc Natl Acad Sci U S A 2011;108:9839–44. doi:1103270108 [pii]10.1073/pnas.1103270108.

[18] Gerard FCA, Ribeiro E de A, Leyrat C, Ivanov I, Blondel D, Longhi S, et al. Modular Organization of Rabies Virus Phosphoprotein. J Mol Biol 2009;388:978–96. doi:10.1016/j.jmb.2009.03.061.

[19] Bruhn JF, Barnett KC, Bibby J, Thomas JMH, Keegan RM, Rigden DJ, et al. Crystal Structure of the Nipah Virus Phosphoprotein Tetramerization Domain. J Virol 2014;88:758–62. doi:10.1128/JVI.02294-13.

[20] Fuxreiter M, Simon I, Friedrich P, Tompa P. Preformed structural elements feature in partner recognition by intrinsically unstructured proteins. J Mol Biol 2004;338:1015–26.

[21] Kingston RL, Hamel DJ, Gay LS, Dahlquist FW, Matthews BW. Structural basis for the attachment of a paramyxoviral polymerase to its template. Proc Natl Acad Sci U S A 2004;101:8301–6.

[22] Blocquel D, Habchi J, Gruet A, Blangy S, Longhi S. Compaction and binding properties of the intrinsically disordered C-terminal domain of Henipavirus nucleoprotein as unveiled by deletion studies. Mol Biosyst 2012;8:392–410. doi:10.1039/c1mb05401e.

[23] Communie G, Habchi J, Yabukarski F, Blocquel D, Schneider R, Tarbouriech N, et al. Atomic Resolution Description of the Interaction between the Nucleoprotein and Phosphoprotein of Hendra Virus. PLoS Pathog 2013;9:e1003631. doi:10.1371/journal.ppat.1003631.

[24] Krumm SA, Takeda M, Plemper RK. The measles virus nucleocapsid protein tail domain is dispensable for viral polymerase recruitment and activity. J Biol Chem 2013;288:29943–53. doi:10.1074/jbc.M113.503862.

[25] Cox RM, Krumm SA, Thakkar VD, Sohn M, Plemper RK. The structurally disordered paramyxovirus nucleocapsid protein tail domain is a regulator of the mRNA transcription gradient. Sci Adv 2017;3:e1602350. doi:10.1126/sciadv.1602350.

[26] Guseva S, Milles S, Jensen MR, Salvi N, Kleman JP, Maurin D, et al. Measles virus nucleo- And phosphoproteins form liquid-like phase-separated compartments that promote nucleocapsid assembly. Sci Adv 2020;6:1–12. doi:10.1126/sciadv.aaz7095.

[27] Zhou Y, Su JM, Samuel CE, Ma D. Measles Virus Forms Inclusion Bodies with

Properties of Liquid Organelles Yuqin. J Virol 2019;93:1–18.

[28] Milles S, Jensen MR, Lazert C, Guseva S, Ivashchenko S, Communie G, et al. An ultraweak interaction in the intrinsically disordered replication machinery is essential for measles virus function. Sci Adv 2018;4:eaat7778. doi:10.1126/sciadv.aat7778.

[29] Sourimant J, Rameix-Welti M-A, Gaillard A-L, Chevret D, Galloux M, Gault E, et al. Fine mapping and characterization of the L-polymerase-binding domain of the respiratory syncytial virus phosphoprotein. J Virol 2015;89:4421–33. doi:10.1128/JVI.03619-14.

[30] Cox R, Plemper RK. The paramyxovirus polymerase complex as a target for next-generation anti-paramyxovirus therapeutics. Front Microbiol 2015;6:1–14. doi:10.3389/fmicb.2015.00459.

[31] Ogino T, Green TJ. RNA Synthesis and Capping by Non-segmented Negative Strand RNA Viral Polymerases: Lessons From a Prototypic Virus. Front Microbiol 2019;10:1–28. doi:10.3389/fmicb.2019.01490.

[32] Morin B, Rahmeh AA, Whelan SP. Mechanism of RNA synthesis initiation by the vesicular stomatitis virus polymerase. EMBO J 2012;31:1320–9. doi:10.1038/emboj.2011.483 emboj2011483 [pii].

[33] Noton SL, Fearns R. Initiation and regulation of paramyxovirus transcription and replication. Virology 2015:1–10. doi:10.1016/j.virol.2015.01.014.

[34] Bloyet LM, Brunel J, Dosnon M, Hamon V, Erales J, Gruet A, et al. Modulation of Re-initiation of Measles Virus Transcription at Intergenic Regions by PXDto NTAILBinding Strength. PLoS Pathog 2016;12:1–39. doi:10.1371/journal.ppat.1006058.

[35] Brunel J, Chopy D, Dosnon M, Bloyet L-M, Devaux P, Urzua E, et al. Sequence of Events in Measles Virus Replication: Role of Phosphoprotein-Nucleocapsid Interactions. J Virol 2014;88:10851–63. doi:10.1128/JVI.00664-14.

[36] Jensen MR, Communie G, Ribeiro Jr. EA, Martinez N, Desfosses A, Salmon L, et al. Intrinsic disorder in measles virus nucleocapsids. Proc Natl Acad Sci U S A 2011;108. doi:10.1073/pnas.1103270108.

[37] Baronti L, Erales J, Habchi J, Felli IC. Dynamics of the Intrinsically Disordered C-Terminal Domain of the Nipah Virus Nucleoprotein and Interaction with the X Domain of the Phosphoprotein as Unveiled by NMR Spectroscopy 2015:268–76. doi:10.1002/cbic.201402534.

[38] Thakkar VD, Cox RM, Sawatsky B, da Fontoura Budaszewski R, Sourimant J, Wabbel K, et al. The unstructured paramyxovirus nucleocapsid protein tail domain modulates viral pathogenesis through regulation of transcriptase activity. J Virol 2018;92.

[39] Shu Y, Habchi J, Costanzo S, Padilla A, Brunel J, Gerlier D, et al. Plasticity in structural and functional interactions between the phosphoprotein and nucleoprotein of measles virus. J Biol Chem 2012;287:11951–67. doi:M111.333088 [pii] 10.1074/jbc.M111.333088.

[40] Bloyet L-M, Schramm A, Lazert C, Raynal B, Hologne M, Walker O, et al. Regulation of measles virus gene expression by P protein coiled-coil properties. Sci Adv 2019;5:eaaw3702. doi:10.1126/sciadv.aaw3702.

[41] Sourimant J, Thakkar VD, Cox RM, Plemper RK. Viral evolution identifies a regulatory interface between paramyxovirus polymerase complex and nucleocapsid that controls replication dynamics. Sci Adv 2020;6. doi:10.1126/sciadv.aaz1590.

[42] Guseva S, Milles S, Jensen MR, Schoehn G, Ruigrok RW, Blackledge M. Structure, dynamics and phase separation of measles virus RNA replication machinery. Curr Opin Virol 2020;41:59–67. doi:10.1016/j.coviro.2020.05.006.

[43] Smallwood S, Ryan KW, Moyer SA. Deletion analysis defines a carboxyl-proximal region of Sendai virus P protein that binds to the polymerase L protein. Virology 1994;202:154–63.

[44] Abdella R, Aggarwal M, Okura T, Lamb RA, He Y. Structure of a paramyxovirus polymerase complex reveals a unique methyltransferase-CTD conformation. Proc Natl Acad Sci U S A 2020;117:4931–41. doi:10.1073/pnas.1919837117.

[45] Du Pont V, Jiang Y, Plemper RK. Bipartite interface of the measles virus phosphoprotein X domain with the large polymerase protein regulates viral polymerase dynamics. PLoS Pathog 2019;15. doi:10.1371/journal.ppat.1007995.

[46] Kingston RL, Gay LS, Baase WS, Matthews BW. Structure of the nucleocapsid-binding domain from the mumps virus polymerase; an example of protein folding induced by crystallization. J Mol Biol 2008;379:719–31.

[47] Blanchard L, Tarbouriech N, Blackledge M, Timmins P, Burmeister WP, Ruigrok RWH, et al. Structure and dynamics of the nucleocapsid-binding domain of the Sendai virus phosphoprotein in solution. Virology 2004;319:201–11. doi:10.1016/j.virol.2003.10.029.

[48] Yegambaram K, Bulloch EMM, Kingston RL. Protein domain definition should allow for conditional disorder. Protein Sci 2013;22:1502–18. doi:10.1002/pro.2336.

[49] Matthews BW. The extension of the isomorphous replacement method to include anomalous scattering measurements. Acta Crystallogr 1966;20:82–6. doi:10.1107/s0365110x6600015x.

[50] Johansson K, Bourhis JM, Campanacci V, Cambillau C, Canard B, Longhi S. Crystal structure of the measles virus phosphoprotein domain responsible for the induced folding of the C-terminal domain of the nucleoprotein. J Biol Chem 2003;278:44567–73.

[51] Krissinel E, Henrick K. Inference of macromolecular assemblies from crystalline state. J Mol Biol 2007;372:774–97.

[52] Bliven S, Lafita A, Parker A, Capitani G, Duarte JM. Automated evaluation of quaternary structures from protein crystals. PLoS Comput Biol 2018;14:1–19. doi:10.1371/journal.pcbi.1006104.

[53] Houben K, Marion D, Tarbouriech N, Ruigrok RW, Blanchard L. Interaction of the C-terminal domains of sendai virus N and P proteins: comparison of polymerase-nucleocapsid interactions within the paramyxovirus family. J Virol 2007;81:6807–16.

[54] Schneider R, Maurin D, Communie G, Kragelj J, Hansen DF, Ruigrok RWH, et al. Visualizing the molecular recognition trajectory of an intrinsically disordered protein using multinuclear relaxation dispersion NMR. J Am Chem Soc 2015;137:1220–9. doi:10.1021/ja511066q.

[55] Diallo A, Barrett T, Barbron M, Meyer G, Lefevre PC. Cloning of the nucleocapsid protein gene of peste-des-petits- ruminants virus - relationship to other morbilliviruses. J Gen Virol 1994;75:233–7. doi:Doi 10.1099/0022-1317-75-1-233.

[56] Habchi J, Mamelli L, Darbon H, Longhi S. Structural disorder within Henipavirus nucleoprotein and phosphoprotein: from predictions to experimental assessment. PLoS One 2010;5:e11684. doi:10.1371/journal.pone.0011684.

[57] Habchi J, Blangy S, Mamelli L, Jensen MR, Blackledge M, Darbon H, et al. Characterization of the interactions between the nucleoprotein and the phosphoprotein of Henipavirus. J Biol Chem 2011;286:13583–602. doi:M111.219857 [pii] 10.1074/jbc.M111.219857.

[58] Erales J, Beltrandi M, Roche J, Maté M, Longhi S. Insights into the Hendra virus NTAIL–XD complex: Evidence for a parallel organization of the helical MoRE at the XD surface stabilized by a combination of hydrophobic and polar interactions. Biochim Biophys Acta - Proteins Proteomics 2015;1854:1038–53. doi:10.1016/j.bbapap.2015.04.031.

[59] Blocquel D, Habchi J, Gruet A, Blangy S, Longhi S. Compaction and binding properties of the intrinsically disordered C-terminal domain of Henipavirus nucleoprotein as unveiled by deletion studies. Mol Biosyst 2012;8:392–410. doi:10.1039/c1mb05401e.

[60] Dimaio F, Terwilliger TC, Read RJ, Wlodawer A, Oberdorfer G, Wagner U, et al. Improved molecular replacement by density- and energy-guided protein structure optimization. Nature 2011;473:540–3. doi:10.1038/nature09964.

[61] Bibby J, Keegan RM, Mayans O, Winn MD, Rigden DJ. AMPLE : a cluster-and-truncate approach to solve the crystal structures of small proteins using rapidly computed ab initio models. Corrigendum . Acta Crystallogr Sect D Biol Crystallogr 2014;70:1174–1174. doi:10.1107/s1399004714006154.

[62] Plevin MJ, Bryce DL, Boisbouvier J. Direct detection of CH/π interactions in proteins. Nat Chem 2010;2:466–71. doi:10.1038/nchem.650.

[63] Marsh JA, Singh VK, Jia Z, Forman-Kay JD. Sensitivity of secondary structure propensities to sequence differences between alpha- and gamma-synuclein: implications for fibrillation. Protein Sci 2006;15:2795–804.

[64] Vallurupalli P, Bouvignies G, Kay LE. Studying “invisible” excited protein states in slow exchange with a major state conformation. J Am Chem Soc 2012;134:8148–61.

doi:10.1021/ja3001419.

[65] Tamiola K, Acar B, Mulder FAA. Sequence-specific random coil chemical shifts of intrinsically disordered proteins. J Am Chem Soc 2010;132:18000–3. doi:10.1021/ja105656t.

[66] Bernado P, Mylonas E, Petoukhov M V, Blackledge M, Svergun DI. Structural Characterization of Flexible Proteins Using Small-Angle X-ray Scattering. J Am Chem Soc 2007;129:5656–64.

[67] Bernadó P, Svergun DI. Structural analysis of intrinsically disordered proteins by small-angle X-ray scattering. Mol Biosyst 2012;8:151. doi:10.1039/c1mb05275f.

[68] Leyrat C, Schneider R, Ribeiro EA, Yabukarski F, Yao M, Gérard FCA, et al. Ensemble structure of the modular and flexible full-length vesicular stomatitis virus phosphoprotein. J Mol Biol 2012;423:182–97. doi:10.1016/j.jmb.2012.07.003.

[69] Bernard C, Gely S, Bourhis JM, Morelli X, Longhi S, Darbon H. Interaction between the C-terminal domains of N and P proteins of measles virus investigated by NMR. FEBS Lett 2009;583:1084–9. doi:10.1016/j.febslet.2009.03.004.

[70] Yegambaram K, Kingston RL. The feet of the measles virus polymerase bind the viral nucleocapsid protein at a single site. Protein Sci 2010;19:893–9. doi:10.1002/pro.354.

[71] Gely S, Lowry DF, Bernard C, Jensen MR, Blackledge M, Costanzo S, et al. Solution structure of the C-terminal X domain of the measles virus phosphoprotein and interaction with the intrinsically disordered C-terminal domain of the nucleoprotein. J Mol Recognit 2010;23:435–47.

[72] Baskakov I, Bolen DW. Forcing thermodynamically unfolded proteins to fold. J Biol Chem 1998;273:4831–4.

[73] Bonetti D, Camilloni C, Visconti L, Longhi S, Brunori M, Vendruscolo M, et al. Identification and structural characterization of an intermediate in the folding of the measles virus X domain. J Biol Chem 2016;291:10886–92. doi:10.1074/jbc.M116.721126.

[74] Bourhis JM, Johansson K, Receveur-Bréchot V, Oldfield CJ, Dunker KA, Canard B, et al. The C-terminal domain of measles virus nucleoprotein belongs to the class of intrinsically disordered proteins that fold upon binding to their physiological partner. Virus Res 2004;99:157–67. doi:10.1016/j.virusres.2003.11.007.

[75] Cox R, Pickar A, Qiu S, Tsao J, Rodenburg C, Dokland T, et al. Structural studies on the authentic mumps virus nucleocapsid showing uncoiling by the phosphoprotein. Proc Natl Acad Sci 2014;111:15208–13. doi:10.1073/pnas.1413268111.

[76] Tuckis J, Smallwood S, Feller JA, Moyer SA. The C-terminal 88 amino acids of the Sendai virus P protein have multiple functions separable by mutation. J Virol 2002;76:68–77.

[77] Kolakofsky D, Le Mercier P, Iseni F, Garcin D. Viral RNA polymerase scanning and the gymnastics of Sendai virus RNA synthesis. Virology 2004;318:463–73.

doi:10.1016/j.virol.2003.10.031.

[78] Curran J. A role for the Sendai virus P protein trimer in RNA synthesis. J Virol 1998;72:4274–80.

[79] Bloyet L-M, Welsch J, Enchery F, Mathieu C, de Breyne S, Horvat B, et al. HSP90 Chaperoning in Addition to Phosphoprotein Required for Folding but Not for Supporting Enzymatic Activities of Measles and Nipah Virus L Polymerases. J Virol 2016;90:6642–56. doi:10.1128/JVI.00602-16.

[80] Madeira F, Park YM, Lee J, Buso N, Gur T, Madhusoodanan N, et al. The EMBL-EBI search and sequence analysis tools APIs in 2019. Nucleic Acids Res 2019;47:W636–41. doi:10.1093/nar/gkz268.

[81] ESPript n.d. http://espript.ibcp.fr.

[82] The UniProt Consortium. UniProt: The universal protein knowledgebase in 2021. Nucleic Acids Res 2021;49:D480–9. doi:10.1093/nar/gkaa1100.

[83] Wyatt PJ. Light scattering and the absolute characterization of macromolecules 1993;272.

[84] Uversky VN. Use of fast protein size-exclusion liquid chromatography to study the unfolding of proteins which denature through the molten globule. Biochemistry 1993;32:13288–98.

[85] Pace CN, Shirley BA, Thompson JA, Rickwood D, Hames BD. Measuring the conformational stability of a protein. In: Creighton TE, editor. Protein Struct. a Pract. approach, Oxford: IRL Press; 1989, p. 311–30.

[86] Franke D, Petoukhov M V, Konarev P V, Panjkovich A, Tuukkanen A, Mertens HDT, et al. ATSAS 2.8: A comprehensive data analysis suite for small-angle scattering from macromolecular solutions. J Appl Crystallogr 2017;50:1212–25. doi:10.1107/S1600576717007786.

[87] Svergun Mylonas, E. DI. Accuracy of molecular mass determination of proteins in solution by small-angle x-rqay scattering. J Appl Crystallogr 2007;40:245–9.

[88] Bernado P, Blackledge M. A self-consistent description of the conformational behavior of chemically denatured proteins from NMR and small angle scattering. Biophys J 2009;97:2839–45.

[89] Graziano V, Mcgrath WJ, Yang L, Mangel WF. SARS CoV Main Proteinase : The Monomer - Dimer Equilibrium Dissociation Constant 2006:14632–41.

[90] Kabsch W. Xds. Acta Crystallogr D Biol Crystallogr 2010;66:125–32. doi:10.1107/S0907444909047337 S0907444909047337 [pii].

[91] Pape T, Schneider TR. HKL2MAP: a graphical user interface for phasing with SHELX programs . J Appl Cryst 2004;37:843–4.

[92] Cowtan K. The Buccaneer software for automated model building. 1. Tracing protein

chains. Acta Crystallogr Sect D Biol Crystallogr 2006;62:1002–11. doi:10.1107/S0907444906022116.

[93] Winn MD, Ballard CC, Cowtan KD, Dodson EJ, Emsley P, Evans PR, et al. Overview of the CCP4 suite and current developments. Acta Crystallogr Sect D Biol Crystallogr 2011;67:235–42. doi:10.1107/S0907444910045749.

[94] Adams PD, Afonine P V, Bunkoczi G, Chen VB, Davis IW, Echols N, et al. PHENIX: a comprehensive Python-based system for macromolecular structure solution. Acta Crystallogr D Biol Crystallogr 2010;66:213–21.

[95] Emsley P, Cowtan K. Coot: model-building tools for molecular graphics. Acta Crystallogr D Biol Crystallogr 2004;60:2126–32.

[96] Murshudov GN, Skubak P, Lebedev AA, Pannu NS, Steiner RA, Nicholls RA, et al. REFMAC5 for the refinement of macromolecular crystal structures. Acta Crystallogr D Biol Crystallogr 2011;67:355–67. doi:10.1107/S0907444911001314 S0907444911001314 [pii].

[97] Chen VB, Arendall 3rd WB, Headd JJ, Keedy DA, Immormino RM, Kapral GJ, et al. MolProbity: all-atom structure validation for macromolecular crystallography. Acta Crystallogr D Biol Crystallogr 2010;66:12–21. doi:S0907444909042073 [pii] 10.1107/S0907444909042073.

[98] Delaglio F, Grzesiek S, Vuister GW, Zhu G, Pfeifer J, Bax A. NMRPipe: a multidimensional spectral processing system based on UNIX pipes. J Biomol NMR 1995;6:277–93.

[99] Vranken WF, Boucher W, Stevens TJ, Fogh RH, Pajon A, Llinas M, et al. The CCPN data model for NMR spectroscopy: Development of a software pipeline. Proteins Struct Funct Genet 2005;59:687–96. doi:10.1002/prot.20449.

[100] Lee W, Tonelli M, Markley JL. NMRFAM-SPARKY: Enhanced software for biomolecular NMR spectroscopy. Bioinformatics 2015;31:1325–7. doi:10.1093/bioinformatics/btu830.

[101] Nolan T, Hands RE, Bustin SA. Quantification of mRNA using real-time RT-PCR. Nat Protoc 2006;1:1559–82. doi:10.1038/nprot.2006.236.

[102] Mathieu C, Guillaume V, Volchkova V a, Pohl C, Jacquot F, Looi RY, et al. Nonstructural Nipah virus C protein regulates both the early host proinflammatory response and viral virulence. J Virol 2012;86:10766–75. doi:10.1128/JVI.01203-12.

Legends for the figures

Figure 1 - Structure of NiV P_{XD}. (A) Schematic representation of the architecture of NiV phosphoprotein (P) and nucleoprotein (N). The black lines represent intrinsically disordered regions (IDRs), red waved lines represent α-MoRE, whereas colored boxes represent structured domains. The green arrows show the known interactions between N and P. The dotted arrows indicate interactions with imprecisely defined binding sites. The orange arrows show the known interactions sites with L. NT_{ARM} = N-terminal arm region of N; N_{NTD} = N-terminal domain of N; N_{CTD} = C-terminal domain of N; CT_{ARM} = C-terminal arm region of N; P_{CM} = N^0 chaperon module of P; P_{MD} = multimerization domain of P; P_{XD} = X domain of P; P_{NTR} and P_{CTR} = N- and C-terminal regions of P. **(B) Sequence alignment of NiV and HeV P_{XD}.** The secondary structure location in the crystal structure of isolated NiV P_{XD} and of the chimeric N_{TAIL}-P_{XD} construct (this study) is shown above the sequences, whereas the secondary structure location in isolated HeV P_{XD} (4HEO.pdb) is shown below the sequences. Yellow and green stars indicate charged and hydrophobic residues involved in the interaction with N_{TAIL}, respectively. Arrows indicate residues involved in the salt-bridge network stabilizing the long helix α2. Sequences alignments were obtained with ClustalW and rendering was done with ESPript 3. **(C) Crystal structure.** Electron density map of the asymmetric unit contoured at 1.8 σ and cartoon representation of the NiV P_{XD} in the crystal structure. The N and C-terminal residues of the molecule are indicated as well as the helix names. Residues 688-690 are shown in gray. **(D) Structural alignment of NiV and HeV P_{XD} crystal structures.** Cartoon representation of NiV P_{XD} is shown in red and that of HeV P_{XD} in wheat. Residues of NiV P_{XD} expected to form the α_2–α_3 loop in a hypothetical canonical 3H bundle are shown in gray, whereas the corresponding α_2–α_3 loop in the structure of HeV P_{XD} is shown in blue. The N and C-terminal residues of the molecule are indicated as well as the helix names. **(E) Close-up of the NiV P_{XD} structure showing the H-bond and salt bridge network that connects helices α_1 and $\alpha_{2\text{-}3}$. (F) Intermolecular hydrogen bonds in the dimer interface.** Cartoon representation of dimeric NiV P_{XD} as present in the crystal structure. One monomer is shown in red and the other in orange. Residues 688-690 are shown in gray, and the side chains of residues S660 and H671 are shown in ball and stick representation and H-bonds are shown in dotted lines.

Figure 2 - Structure of the NiV N_{TAIL}-P_{XD} complex. (A) Sequence alignment of NiV and HeV N_{TAIL} regions. The location of the helix α_N present in the chimeric N_{TAIL}-P_{XD} construct is shown above the sequence. Yellow and green stars indicate residues involved in the interaction with P_{XD} as in Figure 1B. **(B) Schematic representation of the NiV N_{TAIL}-P_{XD} construct. (C) Crystal structure.** The electron density map contoured at 1.8 σ. The cartoon model superimposed on the electron density map shows the P_{XD} model used in the automated molecular replacement method, which excluded N_{TAIL}. **(D) Crystal structure.** Cartoon representation of the chimeric protein in the crystal. P_{XD} is shown in red and N_{TAIL} in blue and the GS linker in green. The green dots show the residues missing in the electron density. **(E) Structural comparison of the chimeric NiV and MeV N_{TAIL}-P_{XD} complexes.** P_{XD} is shown

in red, while N_{TAIL} is colored from N-terminal in blue to C-terminal in red. **(F, G) Close-up of the two sides of the interface between NiV PXD and NTAIL.** Cartoon representation with the side-chains displayed in the ball-and-stick view. The side-chain H-bonds or salt bridges are shown as black dotted lines and the putative π interaction as a purple dotted line.

Figure 3 – NiV and HeV P_{XD} partially unfold in solution. (A) SEC-MALLS. The lines show the chromatograms monitored by refractive index measurement for NiV P_{XD} in red, HeV P_{XD} in blue and RNAse A in grey. The crosses show the MM calculated at each time from the light scattering intensity. Numbers show the calculated weight average molecular masses (M_w). **(B) CD spectra.** The spectra of NiV (in black) and HeV P_{XD} (in red) in 20 mM Tris/HCl pH 7.5, 150 NaCl were measured in a cuvette with a pathlength of 1 mm**. (C) NMR spectroscopy.** Secondary structure propensities (SSP) of NiV P_{XD} calculated from experimental Cα and Cβ chemical shifts. **(D) NMR spectroscopy.** Zoom on the 1H-15N HSQC spectrum showing the resonances of I709. Two conformations (a major and a minor state) are observed in slow conformational exchange on the NMR chemical shift time scale as evidenced by exchange cross peaks. **(E) CEST experiments.** Comparison of the CEST-derived ^{15}N chemical shift differences between the major and minor state and the chemical shift differences between random coil shifts (δ_{ncIDP}) and the experimental ^{15}N chemical shifts of the major state (δ_{major}). **(F) Experimental CEST profiles (displayed as points) for selected residues.** Full drawn lines correspond to a simultaneous analysis of CEST data of residues in the range from 684 to 709 according to a two-site exchange model. **(G) Thermal denaturations monitored by far-UV circular dichroism.** The filled symbols are for unfolding experiments and the open symbols for refolding monitored at 222 nm. The theoretical curves (in red) were drawn for a two-state model assuming that $\Delta C_P = 0$ with the following parameters. For NiV P_{XD}: Tm 42.5 ± 0.3 °C, ΔH^0_{unf} = 25.3 ± 0.4 kcal.mol^{-1}, $[\Theta]_N$ = -25600 ± 500 deg.cm^2.dmol^{-1} at 0 °C, mN = 87 ± 8 deg.cm^2.dmol^{-1}.K^{-1} and $[\Theta]_U$ = -5400 ± 100 deg.cm^2.dmol^{-1}. For HeV P_{XD}: T_m = 53.5 ± 0.2 °C, ΔH^0_{unf} = 35.0 ± 0.7 kcal.mol^{-1}, $[\Theta]_N$ = -26300 ± 500 deg.cm^2.dmol^{-1} at 0 °C, mN = 87 ± 5 deg.cm^2.dmol^{-1}.K^{-1} and $[\Theta]_U$ = -5200 ± 100 deg.cm^2.dmol^{-1}.

Figure 4 - Monomer-dimer equilibrium in solution. (A) SEC MALLS experiments at different NiV P_{XD} concentrations. 50 µL of protein solution were injected onto a Superdex 75 column at initial concentration ranging from 0.5 mg.mL^{-1} (80 µM; black) to 48.0 mg.mL^{-1} (7,600 µM; dark red). **(B) SEC MALLS experiments at different HeV P_{XD} concentrations.** 50 µL of protein solution were injected onto a Superdex 200 column at concentration ranging from 5.00 mg.mL^{-1} (800 µM; green) to 33.00 mg.mL^{-1} (5,200 µM; dark red). **(C) SAXS profiles of NiV P_{XD}.** The SAXS profiles are shown at 2.5 (light red) and 20.0 mg.mL^{-1} (dark red). **(D) Guinier plot for NiV P_{XD}.** Data are shown at 2.5 (blue), 5.0 (green), 10.0 (yellow) and 20.0 mg.mL^{-1} (red). **(E) SAXS profiles of HeV P_{XD}.** The SAXS profiles of P_{XD} are shown at 2.4 mg.mL^{-1} (light blue) and 18.0 mg.mL^{-1} (dark blue). **(F) Guinier plot for HeV P_{XD}.** Data are shown at 2.4 (blue), 4.5 (green), 9.0 (yellow) and 18.0 mg.mL^{-1} (red). **(G) Protein concentration dependence of the radius of gyration (R_g).** The Rg values were

calculated from SAXS data by using the Guinier approximation for HeV (in blue) and NiV P_{XD} (in red). The blue line is for guiding the eyes. **(H) Protein concentration dependence of the molecular mass (MM).** The MM values were calculated from scattering intensity at zero angle (I_0/C). The solid lines represent fits to the Eq. 6 with the following parameters. For NiV: Mmono = 6.4 kDa, K_D = 2.8 ± 0.3 mg.mL^{-1}. For HeV: M_{mono} = 6.4 kDa, K_D > 100 mg.mL^{-1}. **(I) Comparison of the scattering profiles of NiV and HeV P_{XD} at low concentration. (J) SEC-SAXS experiment with NiV P_{XD}.** 50 µL of protein solution were injected onto a Superdex 200 column at an initial concentration 23.8 mg.mL^{-1} and monitored on-line by SAXS. The black line shows the the intensity at zero angle (I_0), which is proportional to both MM and concentration and the red dots show the R_g values calculated from the Guinier approximation at the different time intervals. The vertical red, green and blue lines indicate the frame compared in panels K and L. **(K) Comparison of the scattering profiles at three different elution times. (L) Differences between the scattering profiles at different elution times.**

Figure 5 - SAXS experiments with HeV and NiV P_{XD}. (A-C) - Comparison of NiV P_{XD} theoretical and experimental SAXS curves. The experimental curve obtained for NiV P_{XD} at a concentration of 8.0 mg.mL^{-1} is compared to the theoretical curve calculated for the monomeric 3H bundle form (A), the monomeric 2H form (B) and the dimeric $2H_{Dim}$ form (C). The curves were scaled in order to simply compare their shape and not to take into account differences in molecular mass. The χ values are indicated in red. **(D) - Comparison of HeV P_{XD} theoretical and experimental SAXS curves.** The experimental curve obtained at a HeV P_{XD} concentration of 9.0 mg.mL^{-1} is compared to the theoretical curve calculated for the monomeric 3H bundle form [23]. The curves were also simply scaled. **(E) Conformational ensemble modeling from SAXS data.** The left panel describes the composition of the initial ensemble, which is comprised of seven different sub-ensembles clustered into three sub-ensembles: monomeric 2H conformers, monomeric 3H conformers and dimeric 2H conformers. The bar charts in the right panel show the population distributions of the different sub-ensembles that fitted the curves of HeV P_{XD} at 2.5 mg.mL^{-1} (panel F) and of NiV at four different concentrations (panels G-J). **(F-J) EOM modeling.** In the upper part, the black curve shows the experimental data and the red line the fit obtained with EOM for ensembles of conformers. The χ values are indicated in red. The lower part shows the normalized plot of residuals.

Figure 6 - The interaction of NiV P_{XD} with N_{TAIL} prevents dimerization (A) SEC-MALLS analysis of NiV N_{TAIL}-P_{XD} chimeric protein. The proteins were injected on a S200 column equilibrated at 20°C in 20 mM Tris/HCl buffer at pH 7.5 containing 150 mM NaCl. The lines show the chromatograms monitored by refractive index measurement for NiV N_{TAIL}-P_{XD} in red, NiV P_{XD} in dark red and RNAse A in grey. The crosses show the MM calculated at each time from the light scattering intensity. Numbers show the calculated weight average masses (M_W). **(B) SEC-SAXS analysis of NiV N_{TAIL}-P_{XD} chimeric protein.** The black line shows the intensity at zero angle (I_0), which is proportional to both MM and

concentration, whereas the red points indicate the values of the radius of gyration calculated from the Guinier plots at the different time intervals. **(C) SAXS profile and fit.** The black symbols show the scattering profile obtained by averaging the individual profiles recorded throughout the SEC elution peak shown in Panel B. The inset shows the Guinier plot. The red line shows the theoretical curve calculated by CORAL for the model shown in Figure 8D (χ = 1.20). **(D) Structural model of NiV N_{TAIL}-P_{XD}.** Model generated by CORAL using SAXS data shown in Figure 6C. The structures of P_{XD} in red and N_{TAIL} in blue were taken from the crystal structure of the N_{TAIL}-P_{XD} construct. The green beads indicate the missing residues in the crystal structure that were added by CORAL.

Figure 7 - Cellular assays. (A) Chimeric Nipah virus. The scheme represents the architecture of NiV genome, where the boxes show viral genes. A crosshatched block indicates the location of region encoding P_{XD}. The lower part shows the aligned sequences of NiV and HeV P_{XD} that are part of the two generated recombinant NiV: wild type NIV ($rNIV_{WT}$) and chimeric Nipah virus carrying P_{XD} of HeV ($rNiV_{HeVPX}$). Amino acids differences are shown in italic and underlined. Amino acid positions within P_{XD} correspond to P protein of NiV. Stop codon is shown as asterisk. **(B-C) Virus growth experiments.** Vero E6 and 293T cells were infected with either $rNiV_{WT}$ or $rNiV_{HeV\text{-}PX}$ at an MOI of 0.01. Culture supernatants were collected at 24, 30, 48, 54 and 72 hours post infection (hpi) and analyzed by TCID50 virus titration (B) and the amounts of genome copies were assessed by RT-qPCR (C). **(D) Western blot analysis.** Culture supernatants of 293 T cells infected with either $rNiV_{WT}$ or $rNiV_{HeV\text{-}PX}$ were harvested at the indicated post infection times and subjected to western blot analysis using anti P and anti M antibodies (left panel). Quantification of the protein bands (right panel) was performed using Image Quant software TL D v. 8 (GE Healthcare). The histogram shows the amounts of protein normalized to mock infection. **(E) Northern blot analysis.** Vero E6 cells were infected with either $rNiV_{WT}$ or $rNiV_{HeV\text{-}PX}$ at an MOI of 0.01. Cells were lysed at 48 hours after infection and used for RNA extraction. Equal quantities of RNA were subjected to northern hybridization using biotinylated DNA probes specific to N, P, M, and F genes (left panel). The histogram (right panel) shows relative amount of mRNA normalized with respect to ribosomal 28S RNA. The length of detected RNAs corresponds to known size of viral mRNA for N (2242), P (2704), M (1253), and F (2337), respectively. Two independent infection experiments were performed in triplicate. Box shows the average ± SD of the values. For WB and NB data one representative experiment is presented.

Figure 8 - Statistical dynamics models. (A) Effect of the multimerization of P on binding avidity for a linear lattice of N molecules. K_D = 1 μM, K_{INTRA} = 1. **(B) Effect of the multimerization of P on the apparent dissociation constant.** The curves in panel A were fitted with a simple binding equation. (**C) Effect of partial unfolding of P_{XD} on binding avidity of tetrameric P for a linear lattice of 4 N molecules**. K_d = 1 μM, K_{INTRA} = 1. The grey dotted lines show the curves for monomeric and tetrameric P taken from panel A as

references. The solid lines show the binding curves obtained by varying K_{UNFOLD} as follows: K_{UNFOLD} was 0.1 (Black), 0.4 (in blue), 1 (in green) or 3 (in red). **(D) Effect partial unfolding of P_{XD} on the apparent dissociation constant.** The curves in panel C were fitted with a simple binding equation. The colors code is the same as in panel C and the values of K_{UNFOLD} are indicated above the bars. **(E) Effect of partial unfolding and dimerization of P_{XD} on binding avidity of tetrameric P for a linear lattice of 4 N molecules**. K_d = 1 μM, K_{INTRA} = 1, K_{UNFOLD} = 1. The grey dotted lines show the curves for monomeric and tetrameric P taken from panel A as references. The dotted green line shows the curve for tetrameric P with no dimerization taken from panel C as reference. The solid lines show the binding curves obtained by varying K_{DIMER} as follows: K_{DIMER} was 0.3 (in red), 1 (in magenta) or 3 (in purple). **(F) Effect of partial unfolding and dimerization of P_{XD} on the apparent dissociation constant.** The curves in panel E were fitted with a simple binding equation. The colors code is the same as in panel E and the values of K_{DIMER} are indicated above the bars.

Figure 9. Schematic representation of the conformational equilibrium of P_{XD} and of its interaction with N_{TAIL}. The different conformers of P_{XD} co-existing in solution are labeled ($2H_{DIM}$, 2H, 3H) and the crystal structures of P_{XD} alone and in complex with N_{TAIL} generated in this work are presented at the ends of the diagram and referenced with their PDB code.

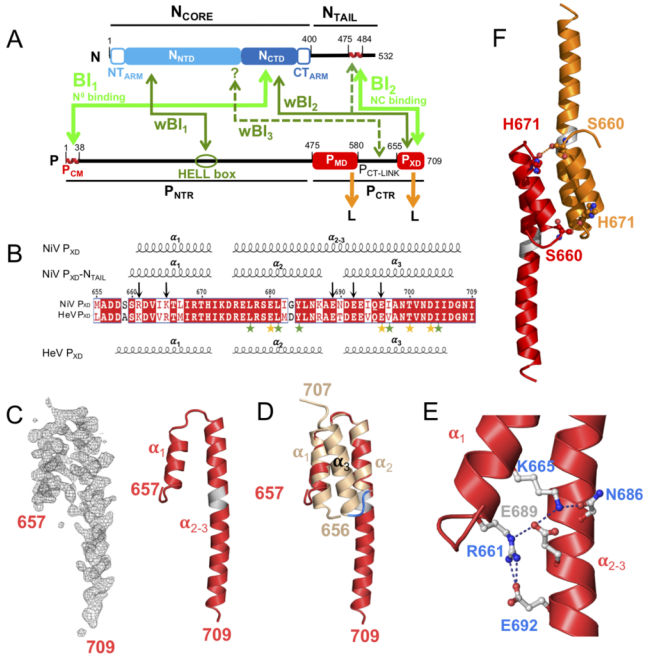
A
N_CORE
N_TAIL
N
N_NTD
N_CTD
NT_ARM
CT_ARM
BI_1
N⁰ binding
BI_2
NC binding
wBI_1
wBI_2
wBI_3
P
P_CM
HELL box
P_MD
P_XD
P_CT-LINK
P_NTR
P_CTR
L
B
NiV P_XD
NiV P_XD-N_TAIL
HeV P_XD
C
D
E
F
H671
S660
K665
N686
E689
R661
E692

Figure 1

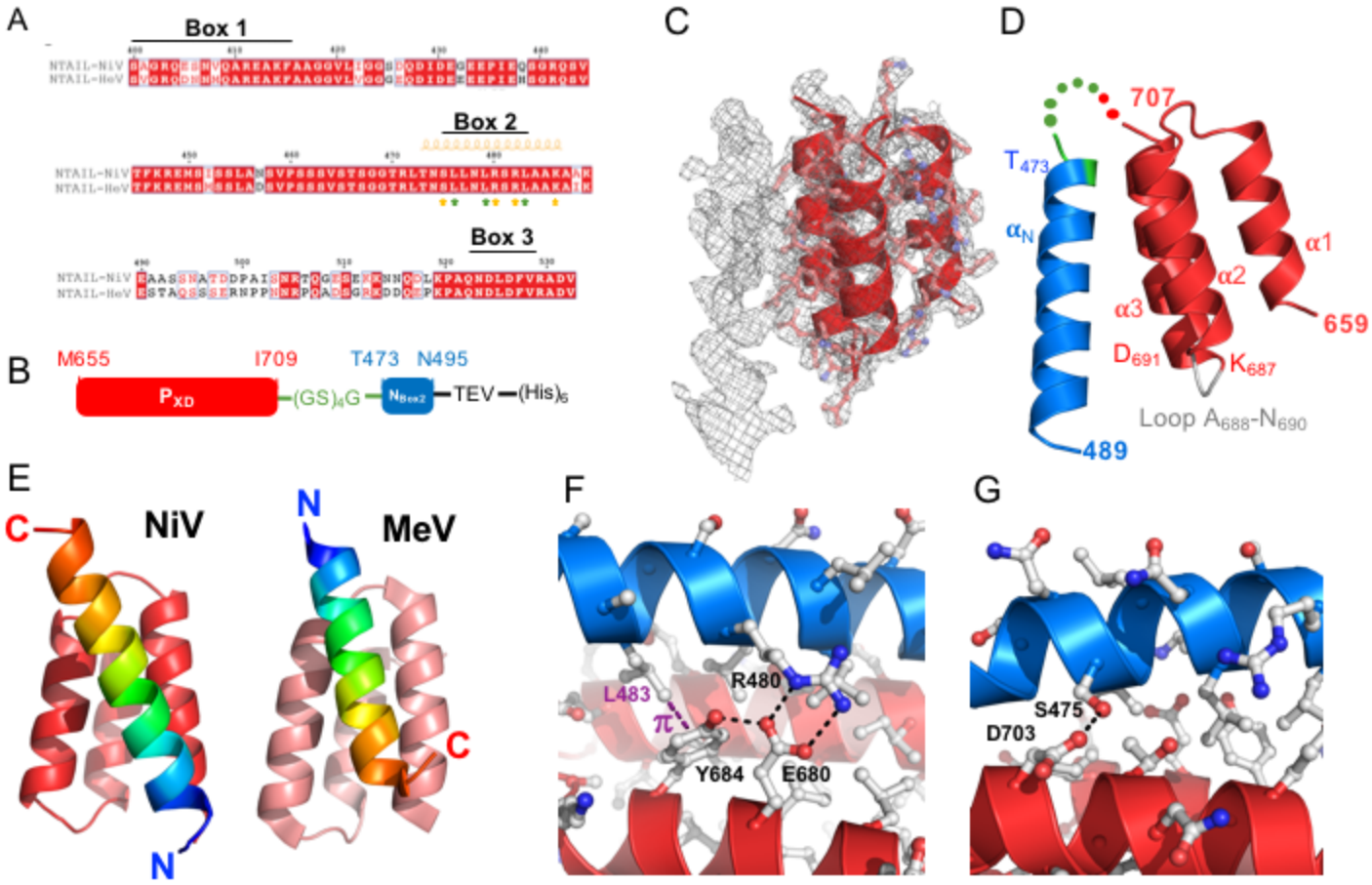
A
Box 1
Box 2
Box 3
B
M655
I709
T473
N495
P_{XD}
$(GS)_4G$
N_{Box2}
TEV
$(His)_6$
C
D
707
T_{473}
α_N
α1
α2
α3
659
D_{691}
K_{687}
Loop A_{688}-N_{690}
489
E
C
NiV
N
N
MeV
C
F
L483
π
R480
Y684
E680
G
S475
D703

Figure 2

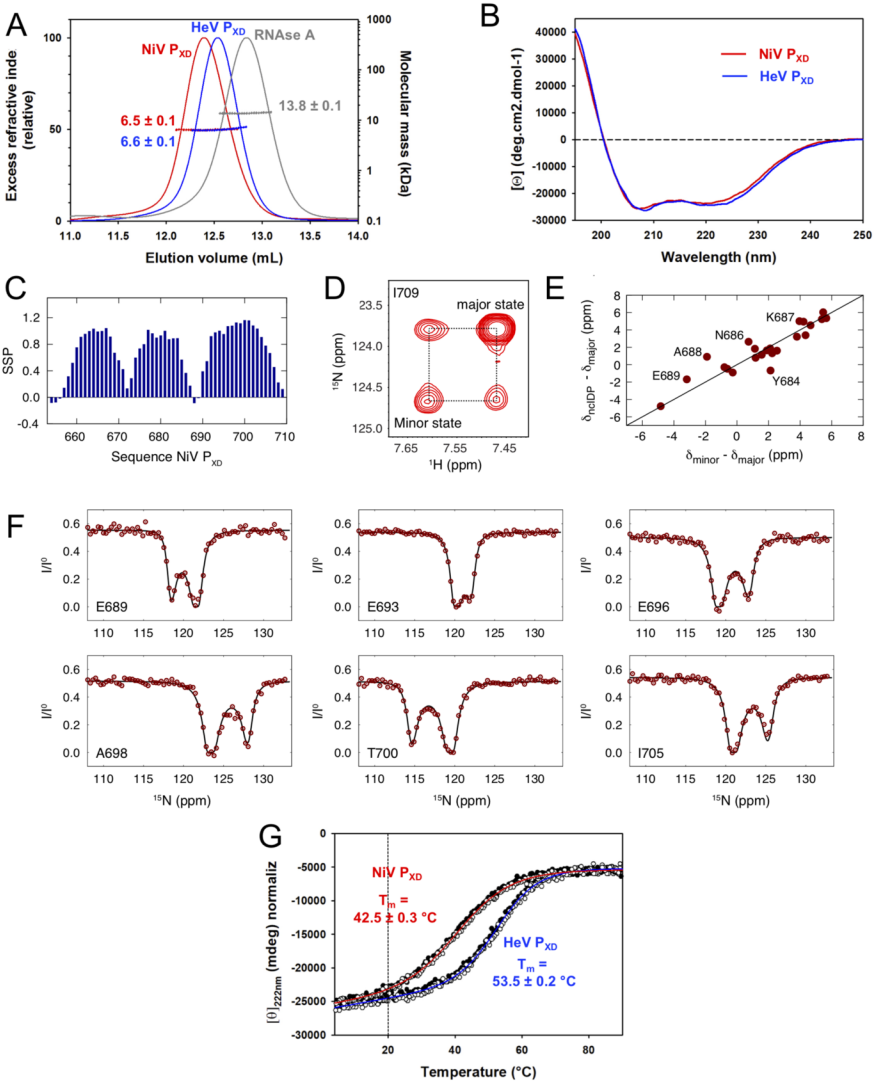
A
HeV P$_{XD}$
NiV P$_{XD}$
RNAse A
13.8 ± 0.1
6.5 ± 0.1
6.6 ± 0.1
Excess refractive inde (relative)
Molecular mass (kDa)
Elution volume (mL)
B
NiV P$_{XD}$
HeV P$_{XD}$
[Θ] (deg.cm2.dmol-1)
Wavelength (nm)
C
SSP
Sequence NiV P$_{XD}$
D
I709
major state
Minor state
^{15}N (ppm)
^{1}H (ppm)
E
K687
N686
A688
E689
Y684
δ$_{ncIDP}$ - δ$_{major}$ (ppm)
δ$_{minor}$ - δ$_{major}$ (ppm)
F
E689
E693
E696
A698
T700
I705
I/I^0
^{15}N (ppm)
G
NiV P$_{XD}$
T$_m$ =
42.5 ± 0.3 °C
HeV P$_{XD}$
T$_m$ =
53.5 ± 0.2 °C
[Θ]$_{222nm}$ (mdeg) normaliz
Temperature (°C)

Figure 3

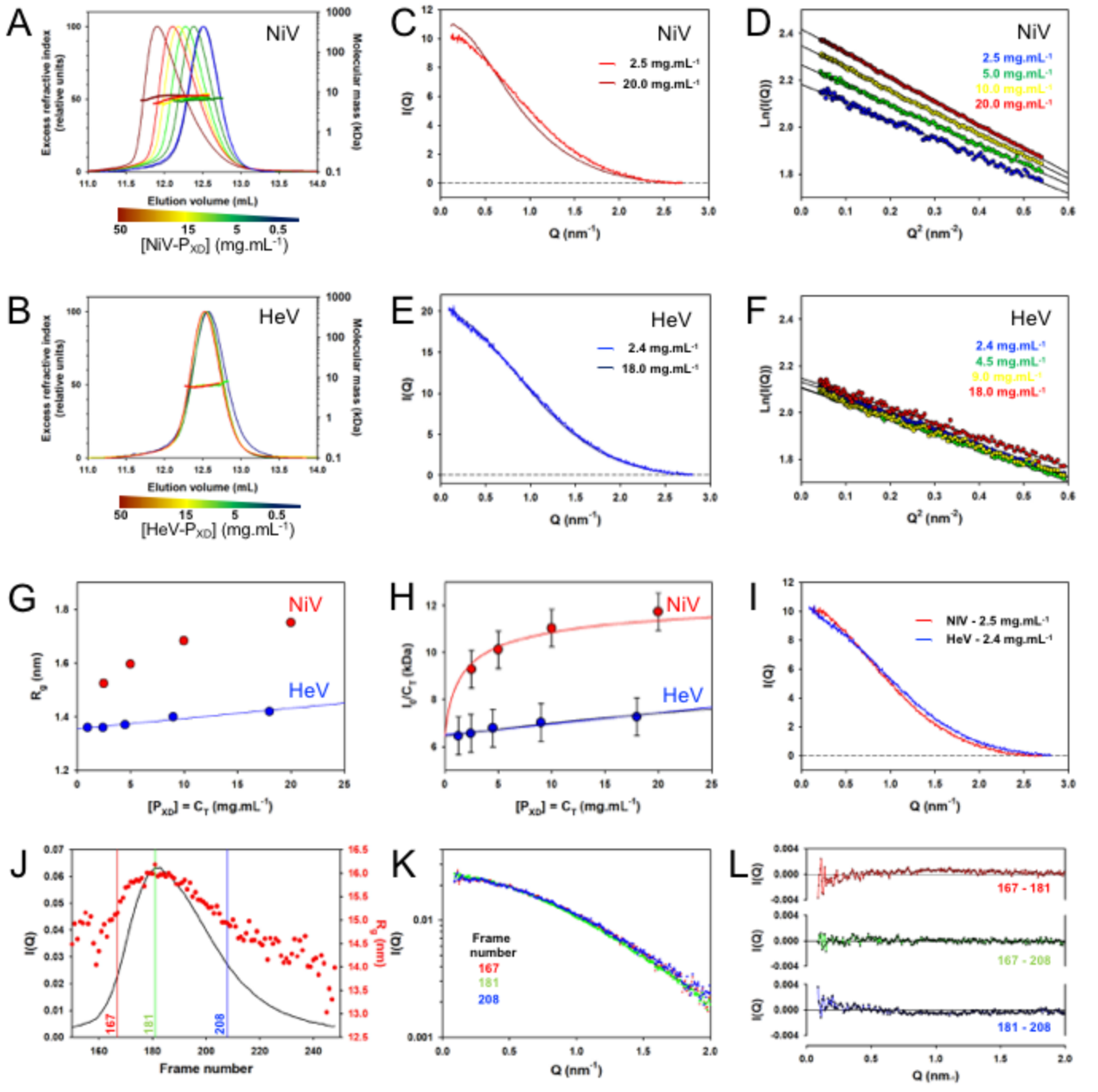
A
NiV
Excess refractive index (relative units)
Molecular mass (kDa)
Elution volume (mL)
[NiV-P$_{XD}$] (mg.mL^{-1})
B
HeV
[HeV-P$_{XD}$] (mg.mL^{-1})
C
NiV
2.5 mg.mL^{-1}
20.0 mg.mL^{-1}
I(Q)
Q (nm^{-1})
D
NiV
2.5 mg.mL^{-1}
5.0 mg.mL^{-1}
10.0 mg.mL^{-1}
20.0 mg.mL^{-1}
Ln(I(Q))
Q^2 (nm^{-2})
E
HeV
2.4 mg.mL^{-1}
18.0 mg.mL^{-1}
F
HeV
2.4 mg.mL^{-1}
4.5 mg.mL^{-1}
9.0 mg.mL^{-1}
18.0 mg.mL^{-1}
G
NiV
HeV
R$_g$ (nm)
[P$_{XD}$] = C$_T$ (mg.mL^{-1})
H
NiV
HeV
I$_0$/C$_T$ (kDa)
[P$_{XD}$] = C$_T$ (mg.mL^{-1})
I
NiV - 2.5 mg.mL^{-1}
HeV - 2.4 mg.mL^{-1}
I(Q)
Q (nm^{-1})
J
I(Q)
R$_g$ (nm)
167
181
208
Frame number
K
Frame number
167
181
208
I(Q)
Q (nm^{-1})
L
I(Q)
167 - 181
167 - 208
181 - 208
Q (nm^{-1})

Figure 4

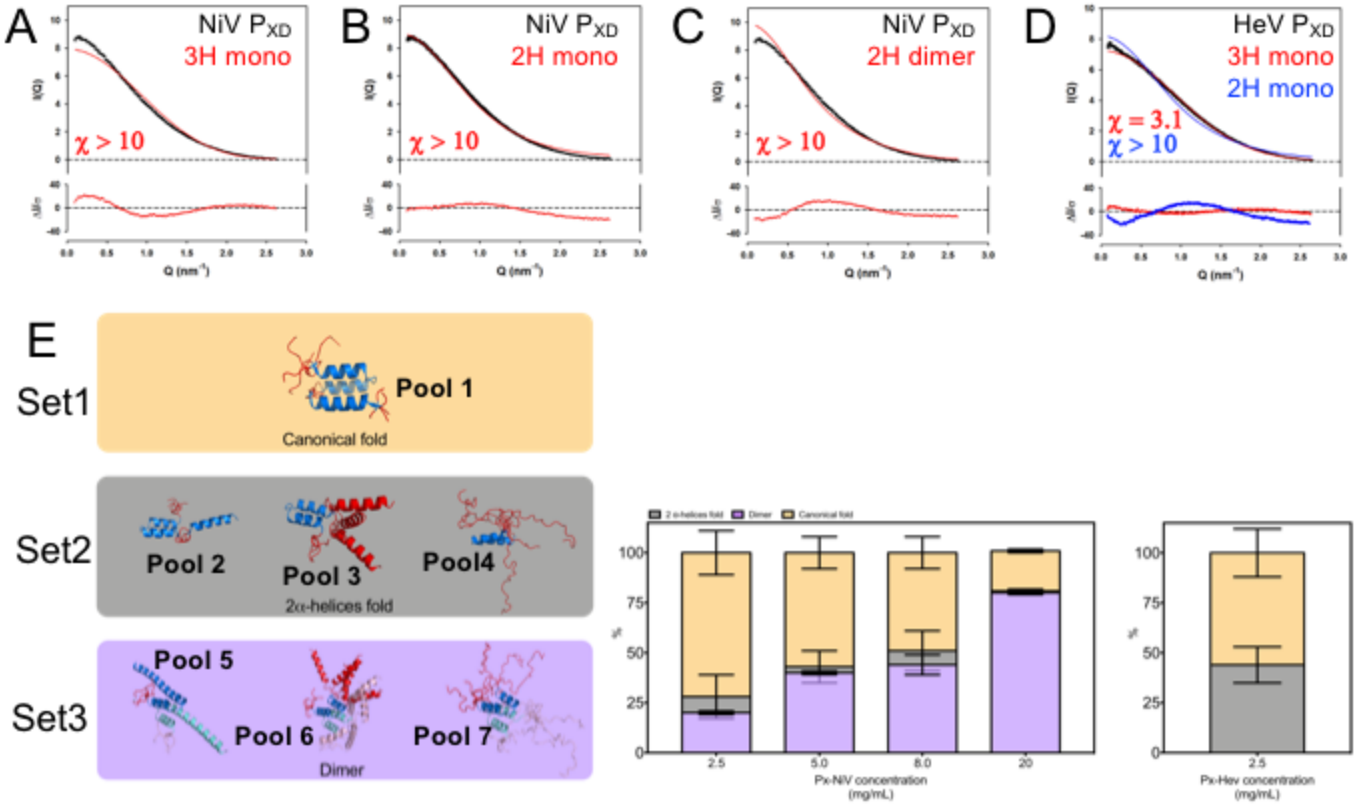
A
NiV PXD
3H mono
χ > 10
B
NiV PXD
2H mono
χ > 10
C
NiV PXD
2H dimer
χ > 10
D
HeV PXD
3H mono
2H mono
χ = 3.1
χ > 10
Q (nm-1)
E
Set1
Pool 1
Canonical fold
Set2
Pool 2
Pool 3
Pool4
2α-helices fold
Set3
Pool 5
Pool 6
Pool 7
Dimer
2 α-helices fold
Dimer
Canonical fold
%
Px-NiV concentration (mg/mL)
Px-Hev concentration (mg/mL)

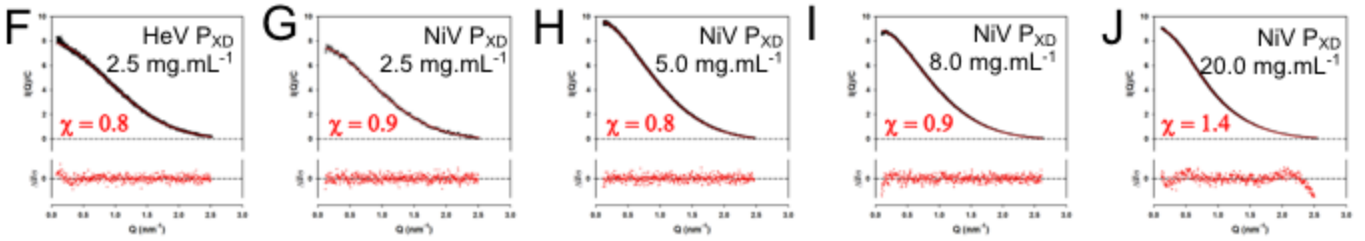
F
HeV PXD
2.5 mg.mL-1
χ = 0.8
G
NiV PXD
2.5 mg.mL-1
χ = 0.9
H
NiV PXD
5.0 mg.mL-1
χ = 0.8
I
NiV PXD
8.0 mg.mL-1
χ = 0.9
J
NiV PXD
20.0 mg.mL-1
χ = 1.4
I(Q)
ΔI/σ
Q (nm-1)

Figure 5

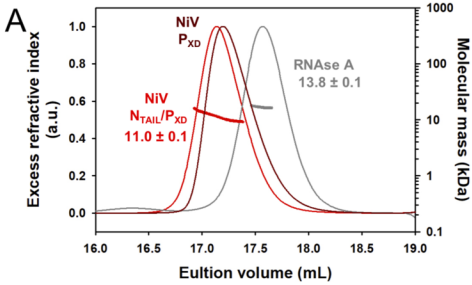
A
NiV
P_{XD}
NiV
N_{TAIL}/P_{XD}
11.0 ± 0.1
RNAse A
13.8 ± 0.1
Excess refractive index (a.u.)
Molecular mass (kDa)
Eultion volume (mL)

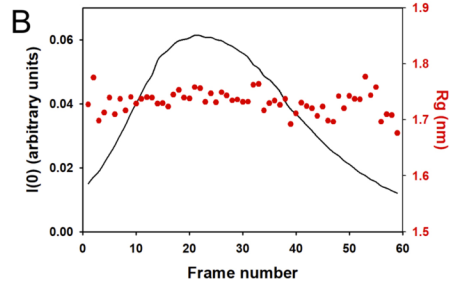
B
I(0) (arbitrary units)
Rg (nm)
Frame number

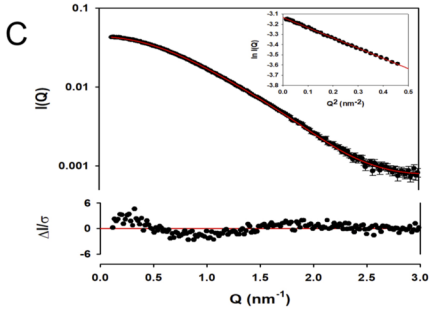
C
I(Q)
ln I(Q)
Q^2 (nm^{-2})
ΔI/σ
Q (nm^{-1})

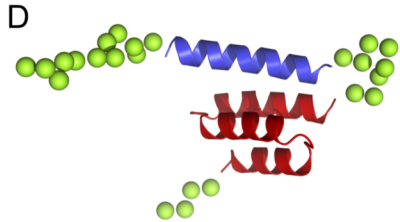
D

Figure 6

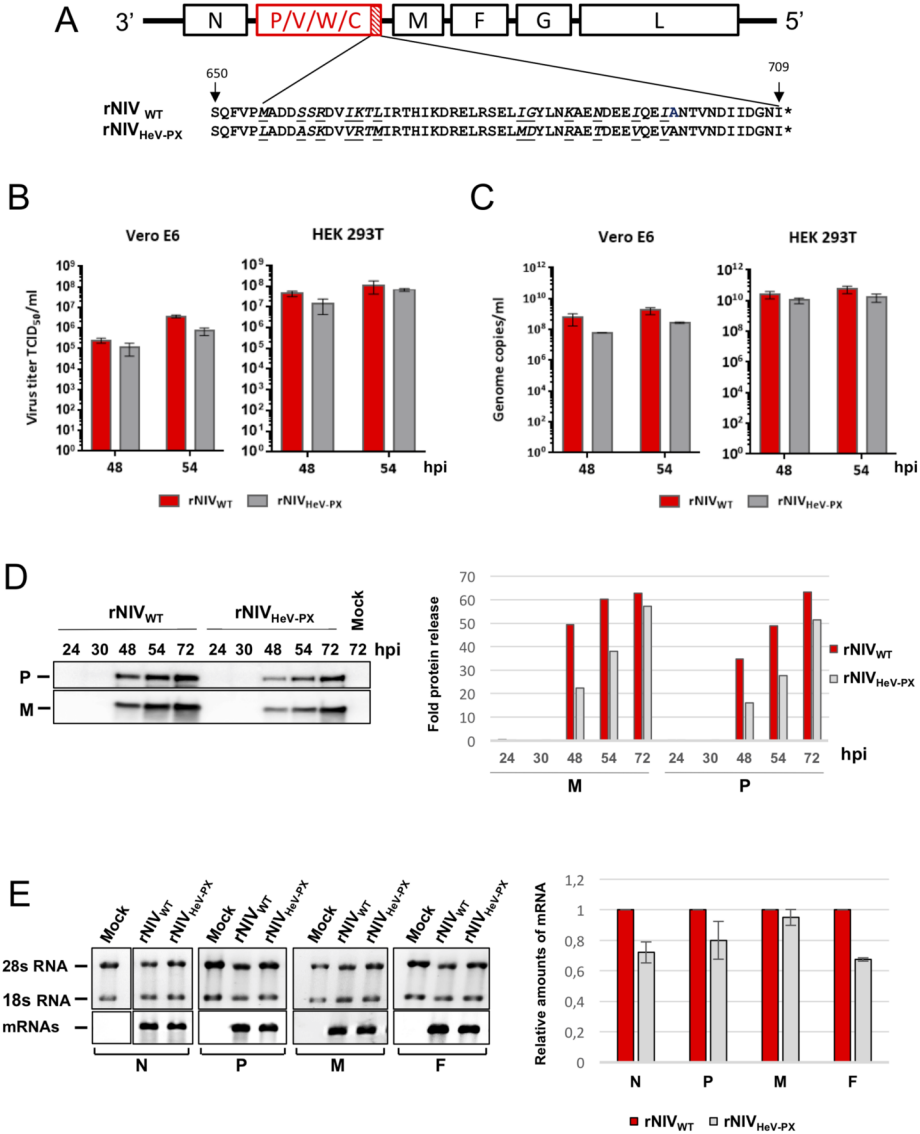
A
3'
N
P/V/W/C
M
F
G
L
5'
650
709
rNIV WT SQFVPMADDSSRDVIKTLIRTHIKDRELRSELIGYLNKAENDEEIQEIANTVNDIIDGNI*
rNIV HeV-PX SQFVPLADDASKDVVRTMIRTHIKDRELRSELMDYLNRAETDEEVQEVANTVNDIIDGNI*
B
Vero E6
HEK 293T
Virus titer TCID50/ml
48
54
hpi
rNIVWT
rNIVHeV-PX
C
Vero E6
HEK 293T
Genome copies/ml
48
54
hpi
rNIVWT
rNIVHeV-PX
D
rNIVWT
rNIVHeV-PX
Mock
24 30 48 54 72 24 30 48 54 72 72 hpi
P
M
Fold protein release
24 30 48 54 72 24 30 48 54 72
hpi
M
P
rNIVWT
rNIVHeV-PX
E
Mock
rNIVWT
rNIVHeV-PX
28s RNA
18s RNA
mRNAs
N
P
M
F
Relative amounts of mRNA
N
P
M
F
rNIVWT
rNIVHeV-PX

Figure 7

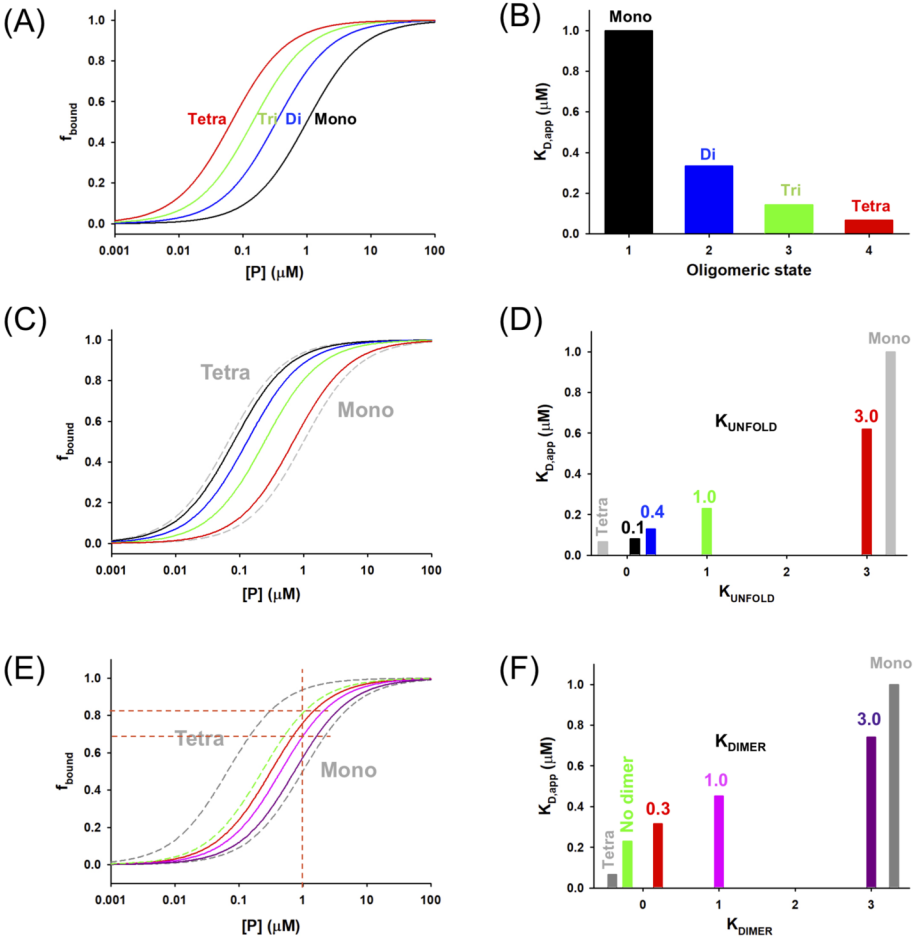
(A)
Tetra
Tri
Di
Mono
f_{bound}
[P] (μM)
(B)
Mono
Di
Tri
Tetra
$K_{D,app}$ (μM)
Oligomeric state
(C)
Tetra
Mono
f_{bound}
[P] (μM)
(D)
Mono
K_{UNFOLD}
3.0
1.0
0.4
0.1
Tetra
$K_{D,app}$ (μM)
K_{UNFOLD}
(E)
Tetra
Mono
f_{bound}
[P] (μM)
(F)
Mono
K_{DIMER}
3.0
1.0
0.3
No dimer
Tetra
$K_{D,app}$ (μM)
K_{DIMER}

Figure 8

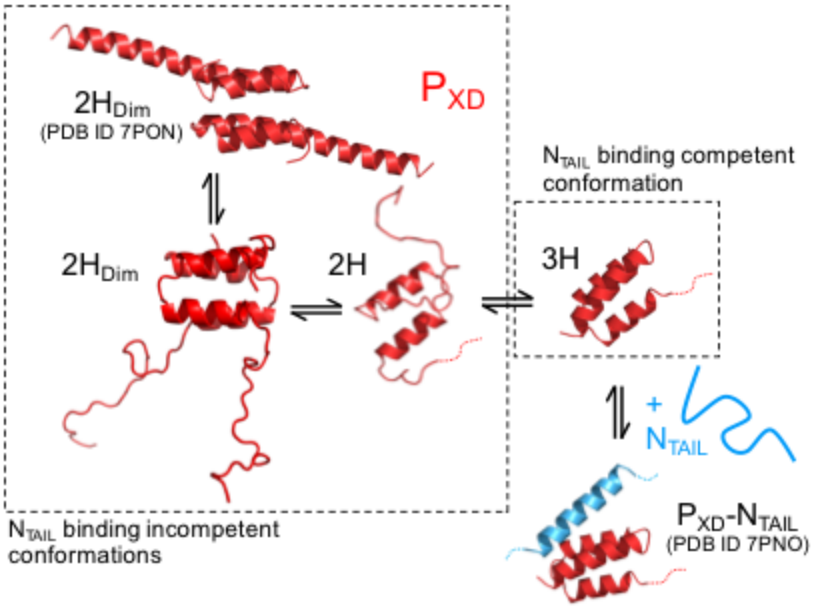
2H$_{Dim}$
(PDB ID 7PON)
P$_{XD}$
2H$_{Dim}$
2H
3H
N$_{TAIL}$ binding competent
conformation
+
N$_{TAIL}$
P$_{XD}$-N$_{TAIL}$
(PDB ID 7PNO)
N$_{TAIL}$ binding incompetent
conformations

Figure 9

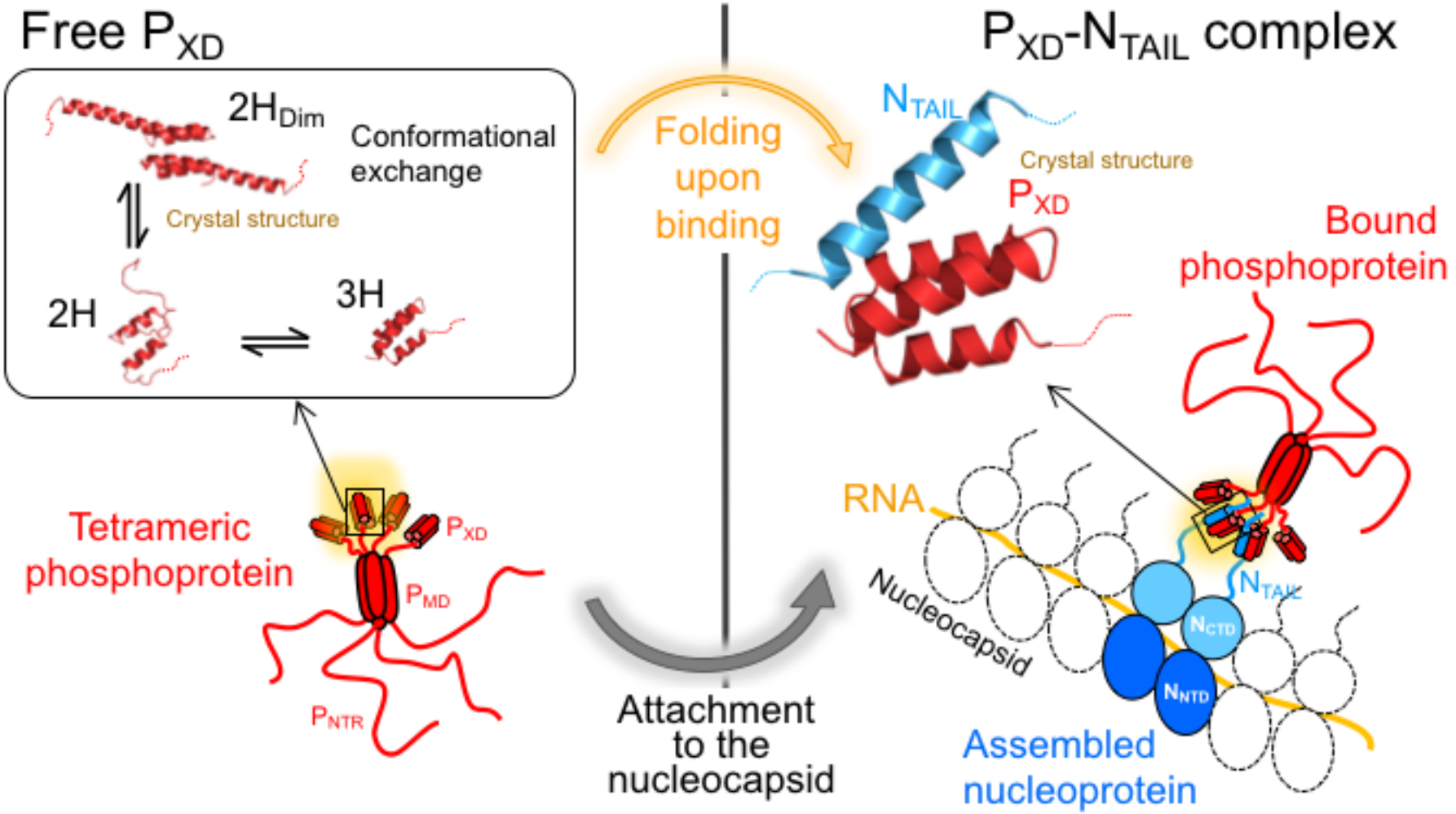
Free P_{XD}
$2H_{Dim}$
Conformational exchange
Crystal structure
2H
3H
Tetrameric phosphoprotein
P_{XD}
P_{MD}
P_{NTR}
Folding upon binding
Attachment to the nucleocapsid
P_{XD}-N_{TAIL} complex
N_{TAIL}
Crystal structure
P_{XD}
Bound phosphoprotein
RNA
Nucleocapsid
N_{TAIL}
N_{CTD}
N_{NTD}
Assembled nucleoprotein